SPECTRUM SENSING FOR
COGNITIVE RADIO NETWORKS

by

Yuandao Sun
A Dissertation
Submitted to the
Graduate Faculty
of
George Mason University
In Partial fulfillment of
The Requirements for the Degree
of
Doctor of Philosophy
Electrical and Computer Engineering

Committee:

_____	Dr. Brian L. Mark, Dissertation Co-director
_____	Dr. Yariv Ephraim, Dissertation Co-director
_____	Dr. Bernd-Peter Paris, Committee Member
_____	Dr. John Shortle, Committee Member
_____	Dr. Monson H. Hayes, Department Chair
_____	Dr. Kenneth S. Ball, Dean, Volgenau School of Engineering

Date: _____ Fall Semester 2015
George Mason University
Fairfax, VA

Spectrum Sensing for Cognitive Radio Networks

A dissertation submitted in partial fulfillment of the requirements for the degree of
Doctor of Philosophy at George Mason University

By

Yuandao Sun
Master of Science
Tongji University, 2011
Bachelor of Science
Zhejiang Gongshang University, 2008

Co-director: Brian L. Mark, Professor
Co-director: Yariv Ephraim, Professor
Department of Electrical and Computer Engineering

Fall Semester 2015
George Mason University
Fairfax, VA

Dedication

I dedicate this dissertation to my heavenly father, my parents, Shaobao Sun and Xiaohua Zhao, and my three sisters, Anna Sun, Changchun Sun and Lasa Sun.

Acknowledgments

I would like to thank my advisors, Professor Brian L. Mark and Professor Yariv Ephraim, for being such amazing advisors throughout my four years research in George Mason University. They have provided me with their in-depth technical knowledge and invaluable research skills. Meanwhile, they also provided me research assistant scholarship to cover some of my living expense. They have always been supportive and patient which has sustained me throughout this unforgettable journey. I am much in debt for their time, expertise, and advice as well as their constructive feedback to make this the best possible dissertation.

I would like to thank my committee members, Professor Bernd-Peter Paris and Professor John Shortle, who have reviewed the dissertation carefully, provided thoughtful suggestions, and challenged me with insightful questions. I would like to thank Professor Andre Manitius, who recruited me into the Electrical and Computer Engineering department and recommended me for the three-year Presidential Scholarship, which supported me during the academic years from 2011-2014. I received financial support during summer 2011 and 2012 from NSF Grant CCF-0916568. I was supported as a graduate research assistant in summer 2013 by a grant from NIST. I would like to acknowledge NSF Grant CNS-1421869, which funded my graduate research assistantships during the academic year 2014-2015, summer 2015, and fall 2015.

I would like to express my appreciation to all faculty and staff in the Electrical and Computer Engineering department for their support, encouragement and candid advice. I will forever treasure the friendships with Thao, Netshat, Zhuxuan and other classmates in the Network Architecture and Performance Lab (NAPL).

Finally, I want to thank my family. I would not have accomplished this milestone without their unconditional love, support, and encouragement. They have given me much needed strength to overcome any obstacles, I am forever obliged.

Table of Contents

List of Tables

List of Figures

viii

Abstract

SPECTRUM SENSING FOR COGNITIVE RADIO NETWORKS

Yuandao Sun, PhD

George Mason University, 2015

Dissertation Co-director: Dr. Brian L. Mark

Dissertation Co-director: Dr. Yariv Ephraim

Cognitive radio has been proposed as a technology for reclaiming highly under-utilized spectrum resources to satisfy the increasing spectrum demand. In a cognitive radio network, unlicensed or secondary users (SUs) are permitted to make use of portions of a licensed spectrum band that are left idle by the licensed or primary users (PUs). These idle portions of spectrum, called spectrum holes, exist in the dimensions of space, time, and frequency. In this thesis, we develop mathematical models and algorithms for detecting spectrum holes in a fixed frequency band, which are characterized either in space or in time.

For spatial spectrum sensing, we assume a model in which the SUs are geographically distributed according to a Poisson point process and the SUs employ a listen-before-talk spectrum access scheme. We derive the moment generating function of the aggregate interference due to the simultaneous transmissions of the SUs. Based on the analysis of the aggregate interference, we propose a power control scheme to allow each SU to transmit with its own power while ensuring that the aggregate interference to the PU is tolerable. In addition, a contention control scheme based on carrier sense multiple access is adopted to avoid collisions between SUs.

We develop algorithms for temporal spectrum sensing of a given frequency channel based

on a hidden bivariate Markov model (HBMM) to describe the active/idle channel occupancy behavior of the PU. The HBMM extends the more traditional hidden Markov model (HMM) by allowing for more general state sojourn time distributions of the PU in each state. The higher degrees of freedom afforded by the HBMM can provide higher modeling fidelity than the HMM, which results in better detection performance. We develop an online algorithm to estimate the HBMM parameter and recursions for estimating and predicting the state of the PU. We then extend the temporal spectrum sensing approach to a collaborative setting in which multiple SUs sense a given frequency channel for spectrum holes to provide better detection performance by exploiting spatial diversity. We develop two HBMM-based collaborative sensing schemes: a soft fusion scheme and a hard fusion scheme. The soft fusion scheme outperforms an optimal linear soft fusion scheme proposed previously in the literature. The hard fusion scheme performs nearly as well as an optimal linear soft fusion scheme when an accurate estimate of the HBMM parameter is available, while incurring much lower communication overhead than soft fusion.

Chapter 1: Introduction

1.1 Motivation

In wireless networks, available spectrum resource has become more and more scarce due to the explosive development of wireless communications. However, spectrum studies show that significant portions of spectrum resource are highly under utilized. In November 2002, the Federal Communications Commission (FCC) published a report aiming to improve the utilization of spectrum resource [12]. This report pointed out that cognitive radio can be considered to be a feasible solution to address the spectrum inefficiency problem.

Therefore, in the past decade, many efforts have been made to develop cognitive radio. For example, in the next generation (XG) program sponsored by the Defense Advanced Research Project Agency (DARPA), the dynamic spectrum access technology was adopted to dynamically redistribute allocated spectrum. In addition, many other projects and experimental platforms have been designed to implement cognitive radio, such as the open access research (WARP) platform designed by Rice University [42], XG Radio designed by the Shared Spectrum Company [36], and a cognitive radio system based on the Long Term Evolution (LTE) framework [24]. Meanwhile, IEEE 802.22 Wireless Regional Area Networks (WRANs) also adopts cognitive radio technology to exploit TV white space aiming to bring broadband access in rural and remote areas. These research and development efforts are making cognitive radio more attractive and achievable.

The definition of cognitive radio adopted by FCC [12], is "a radio or system that senses its operational electromagnetic environment and can dynamically and autonomously adjust its radio operating parameters to modify system operations so as to maximize throughput, mitigate interference, facilitate interoperability, access secondary markets". Cognitive radio is able to perform dynamic spectrum access which has the potential to improve spectrum

utilization by allowing next generation mobile networks access to the attractive radio frequency spectrum bands. Generally speaking, dynamic spectrum access strategies can be broadly categorized into three models [60]: (1) Dynamic exclusive use model: This model maintains the basic structure of the current spectrum regulation policy. The main idea is to introduce flexibility to improve spectrum efficiency with dynamic spectrum resource assignment, but spectrum bands are licensed to services for exclusive use. (2) Open sharing model: This model employs open sharing among peer users as the basis for managing a spectral region. (3) Hierarchical access model: This model adopts a hierarchical access structure with PUs (licensed users) and SUs (unlicensed users). The basic idea is to open licensed spectrum to secondary users while limiting the interference perceived by the PUs. Compared to the dynamic exclusive use and open sharing models, the hierarchical model is perhaps most compatible with the current spectrum management policies and legacy wireless systems, so the hierarchical access model is adopted in this thesis.

In the hierarchical access model, cognitive radio technology must enable communication between SUs without sacrificing the performance of PUs. Specifically, cognitive radio should provide the following functions [3]: (1) Spectrum sensing: Detect and determine which portions of the spectrum are available for SUs usage without causing harmful interference to the PUs. (2) Spectrum management: Select the best available spectrum to meet communication requirements. (3) Spectrum sharing: Coordinate spectrum access among coexisting users with fairness, and also to avoid collision. (4) Spectrum mobility: SUs have to vacate the spectrum immediately when the transmission of PUs is detected.

1.2 Problem statement

Reliable spectrum sensing is the prerequisite of cognitive radio technology. Various approaches for spectrum sensing have been studied in the literature including energy detector, matched filter detector, and cyclostationary detector (cf. [59]). The non-coherent energy detector is the simplest approach to make detection decision by comparing the received

energy to a given threshold. The coherent detector, also referred to as a matched filter, can improve detection performance if knowledge of the transmitted signal is available in the first place. The cyclostationary feature detector can use the inherent periodicity of primary signals for more accurate detection at low SNR, and it is also able to distinguish different types of signals, but it is more computationally demanding and typically requires long sensing intervals.

The basic task of spectrum sensing is to detect available spectrum holes for SUs. A spectrum hole is defined as a band of frequencies assigned to a PU, but this band is not being used by that PU at a particular time or at a specific geographic location. In [59], it has been pointed out that spectrum holes can be explored in several domains. From a spatial point of view, available spectrum may exist in some parts of the geographical area while it is occupied in some other parts by the PUs. From a temporal point of view, available spectrum may exist if the frequency band is not continuously used. In addition, spectrum holes can also be exploited in the frequency, code and angle domains.

In this thesis, we focus on spatial spectrum sensing and temporal spectrum sensing to exploit spectrum holes in the spatial and temporal domains, respectively. In spatial spectrum sensing, interference analysis and power control are the main challenges in order to avoid harmful interference to PUs while maximizing the network throughput. In temporal spectrum sensing, accurate detection of the idle frequency band which is not occupied by PUs is critical. Besides, in order to avoid collisions, the durations of idle periods should be estimated, to allow the SU to return spectrum resource to PU before it reactivates again. Furthermore, collaborative spectrum sensing should be considered because the spectrum sensing performance may degrade severely when the transmitted signal is attenuated by path loss, shadowing, and small scale fading. Efficient collaboration or cooperation between cognitive radios can improve the spectrum sensing performance by exploiting spatial diversity.

1.3   Thesis Contributions

The main contributions of the thesis are summarized as follows:

- We develop a spatial spectrum sensing model by adopting the framework from [41] in which all SUs are scattered in the Euclidean plane according to a Poisson point process. All transmissions are assumed to be omnidirectional, and the signal propagation follows a lognormal shadowing model which includes path loss and lognormal shadowing. We consider a single primary transmitter located in the center of the plane, together with a population of SUs which employ the Listen-Before-Talk dynamic spectrum access scheme (see, e.g., [28,29]). Based on this model, the aggregate interference is quantified in several scenarios. We first consider a scenario in which all SUs transmit with fixed transmission power during the talk phase. With this assumption, we derive the moment generating function and expectation of the aggregate interference. Then, a power control scheme for SUs is proposed based on the aggregate interference analysis . A group maximum interference free transmit power (G-MIFTP) is determined for each SU by taking the tolerable interference threshold of the primary receiver into account. Moreover, we adopt the CSMA/CA multiple access scheme to avoid the collision between SUs.

- We develop an online parameter estimation algorithm for the HBMM and apply it to temporal spectrum sensing. The proposed online HBMM parameter estimator is based on a block-recursive parameter estimation scheme originally developed by Rydén for HMMs [47]. We adopt a method from Willy *et al.* [58] to recursively estimate the score function of the HBMM, and optimize the projection mapping of the online algorithm. Together with the state estimation and prediction recursions presented in [40], the HBMM parameter estimator forms the basis for a fully online scheme for temporal spectrum sensing. The estimation and prediction accuracy of this scheme is comparable to that of the offline Baum-based parameter estimator in [40]. Since the estimator is recursive, it can adapt to slow changes in the statistical behavior of the

PU's transmission pattern.

- We develop collaborative spectrum sensing based on the HBMM and its associated state and parameter estimation algorithms. Compared to collaborative sensing methods that do not employ a model for the temporal dynamics of the PU, the proposed schemes provide superior spectrum detection performance. Our proposed collaborative spectrum sensing schemes can be divided into hard fusion schemes and soft fusion schemes. In the hard fusion scheme, each SU individually performs online state and parameter estimation for an HBMM and the individual decisions are fused using the linear fusion rule of [44] wherein the weights for linear combination are computed as part of the parameter estimation process. Furthermore, a soft fusion scheme is proposed to perform online parameter estimation and state prediction, based on an HBMM with vector observations. The effect of coarse quantization of the observation samples is studied to reduce the network overhead.

1.4   Thesis Outline

The remainder of the thesis is organized as follows. In Chapter 2, we provide a background and literature review for spatial spectrum sensing, temporal spectrum sensing, and collaborative spectrum sensing. In Chapter 3, we investigate spatial spectrum sensing, and analyze the aggregate interference. Then we propose a power control scheme and contention control scheme to maximize the network capacity and limit the interference to the primary system. In Chapter 4, we investigate temporal spectrum sensing and adopt the HBMM to model the channel occupancy behavior. An online parameter estimation algorithm is developed to perform parameter estimation and prediction. In Chapter 5, we investigate collaborative spectrum sensing as a means to overcome the hidden terminal problem. The HBMM hard and soft fusion schemes are studied to improve the spectrum sensing accuracy and reliability. In Chapter 6, we summarize the thesis contributions and discuss possible extensions of our work.

Chapter 2: Background and Literature Review

In recent years, there have been many research activities on cognitive radio and dynamic spectrum access. In this chapter, we would review related works in spatial spectrum sensing, temporal spectrum sensing, and collaborative spectrum sensing.

2.1 Interference and power control

Spatial spectrum sensing is an approach used to detect unused spectrum holes in a geographic area. The technical challenges of spatial spectrum sensing are in large part due to the uncertainty associated with the interference in the network. Such uncertainty can result from the unknown number of SUs and PUs and unknown locations of the SUs and PUs as well as channel fading, shadowing, and other uncertain environment-dependent conditions. Therefore, it is crucial to incorporate such uncertainty in the statistical interference model in order to quantify the effect of interference on the primary system [7, 45]. Interference modeling of cognitive networks differs from that of conventional networks due to the distinct transmission characteristics of a cognitive transceiver. A conventional terminal transmits with a constant power, but a cognitive transceiver is able to optimize its transmission according to the radio environment. For example, in an interference region cognitive radio is not allowed to transmit.

A mathematical framework for characterizing interference in a cognitive radio network was proposed in [41]. In this framework, SUs are scattered in the Euclidean plane according to a Poisson point process and operate asynchronously in a wireless environment subject to path loss, shadowing, and multipath fading. Poisson point processes are widely used in diverse fields such as astronomy, positron emission tomography, cell biology, optical communications, and wireless communications. Although in [41] the aggregate interference

6

from the SUs and its impact on the performance of the primary transmitter are quantified, this paper did not address the problem of how to take advantage of this interference analysis to carry out power control.

The main objectives of power control in conventional wireless networks are to improve the energy efficiency by appropriately reducing the transmission power without degrading the link throughput and to increase the total throughput of the network by enhancing the spatial reuse of the channel. Power control in cognitive radio networks have been studied under different network setups and various performance measures, but the design tradeoffs in conventional power control can still be found here [46]. In [6,50], the authors considered power control of cognitive radio under a fading wireless channel, and proposed an approach to opportunistically adapt the transmission power to allow the secondary users to maximize their achievable transmission rates without degrading the outage probability of the primary user. In [20], Habibul also studied the problem of joint power control and beamforming with the objective of minimizing the total transmitted power of the secondary users such that the interference to the primary user would remain below a threshold level.

In [34], power control is carried out to ensure that a cognitive radio's transmit power does not exceed a maximum interference-free transmit power (MIFTP), which is defined as the maximum power at which a given SU can transmit without causing harmful interference to any of the primary receivers. The MIFTP for the SU is estimated based on signal strength measurements taken by a group of SUs. However, this is done under the assumption that the SUs have the knowledge of their exact locations, and can exchange their observation and transmission decisions with negligible delay. Moreover, it is assumed that at most one SU can transmit at a given time. In practice, due to the uncertainty of the number and locations of SUs as well as channel fading, shadowing, and other uncertain environment-dependent conditions, the communication performance of the PUs may be seriously affected by the aggregate interference generated by multiple SUs transmitting simultaneously [45]. Thus, accurate modeling of the aggregate interference is crucial to designing a cognitive radio network and quantifying the effect of the interference on the performance of the primary

7

system. These issues will be addressed in Chapter 3.

2.2 Model based temporal spectrum sensing

In temporal spectrum sensing, the PU alternates between an active state, in which it transmits a signal onto the channel, and an idle state. The objective of temporal spectrum sensing in a narrowband channel is not only to infer the current state of the PU by monitoring the received signal, but also to forecast the future state of the PU. None of the aforementioned spectrum sensing approaches such as energy detection, matched filter detection, and cyclostationary feature detection, provides such forecasting capability. By anticipating in advance that the PU will change from the idle state to the active state, a cognitive radio could vacate the channel well before such an event occurred, thereby reducing the potential interference to the PU.

Model-based temporal spectrum sensing is considered to enable forecasting the state of PU. Much of the prior work on model-based temporal spectrum sensing relies on the more traditional univariate Markov chain, either in discrete-time or continuous-time, to model the PU. Several papers have used the standard HMM to jointly model the PU state and the effect of the channel. A recent paper by Li *et al.* [30], develops a sequential particle filtering approach for joint estimation of the current state of the PU and of the channel. In [30], a two-state discrete-time Markov chain model for the PU is assumed and the channel is modeled by a finite state Markov chain to characterize time-variant small-scale fading. Empirical results presented in [13, 40] provide evidence of the non-geometric nature of the active and idle periods of a PU. In [13], a continuous-time semi-Markov process was proposed as a model for the PU.

In [40], an approach to model-based temporal spectrum sensing was proposed based on a hidden bivariate Markov model (HBMM). In this context, the HBMM consists of an underlying bivariate Markov chain which models the state sequence of the PU, together with an observation model which characterizes the lognormal shadow fading of the channel between the PU and the cognitive radio. A key benefit of the HBMM for the spectrum

sensing application is that the sojourn times of the PU in the active and idle states are modeled by discrete phase-type distributions, whereas in an HMM the model for sojourn times is limited to the geometric distribution. The ability of the HBMM to characterize general state sojourn times is important for accurate prediction of the future state of a PU.

Parameter estimation for model-based temporal spectrum sensing is crucial. Its estimation accuracy and converge speed directly affect the temporal spectrum sensing performance. In [40], the Baum algorithm [5] is applied to training data to estimate the HBMM parameter. The HBMM parameter estimate is then used to perform state estimation and prediction via forward recursions. This approach was shown to perform well on real spectrum measurement data with respect to estimation and prediction error probabilities. Due to the offline nature of the Baum algorithm, however, it cannot adapt to changes over time in the wireless channel or in the underlying statistics of the PU transmission pattern.

It is desirable to estimate the parameter of the HBMM online. There are several existing algorithm to estimate the parameter of an HMM online. The problem of recursively estimating the parameter of an HMM was first studied by Kashyap in [21], who estimated the elements of the hidden Markov chain transition matrix using noisy measurements of the chain state as the observation sequence. The noise superimposed upon the state signal was assumed to have a zero mean, finite variance, and to be independent of the individual states of the hidden chain. Convergence of the resulting sequence of recursive estimates to the true model parameter was proved under certain conditions. Inspired by the recursive ML-estimator for mixtures algorithm in the independent case combined with the conditioning step in the EM algorithm, Holst and Lindgren proposed a recursive algorithm to estimate the parameter of the hidden Markov model in [19]. In this algorithm the information matrix is required in order to calculate the adaptive matrix in the initial phase of the algorithm, which requires a long sequence of observation data in advance. In 1997, LeGland and Mevel proposed a recursive identification algorithm for a HMM having a hidden discrete-time Markov chain and observations in a discrete alphabet [27]. Further, they addressed consistency issues and convergence of the algorithm to a set of points which locally optimizes a

contrast function. Krishnamurthy and Moore [25] also studied recursive estimation of the parameter of an HMM using a gain matrix which approximates the inverse of the complete data information matrix, and where the model being estimated is assumed to include a discrete-time Markov chain.

In [47], Ryden argued that the Holst-Lindgren algorithm locally minimized the relative entropy rate and yielded asymptotically normal estimates under some general conditions. Ryden also proposed a recursive estimator for the hidden Markov model based on the m-dimensional distribution of the process and showed that this estimator converges to the set of stationary points of the corresponding Kullback-Leibler information. As we will discuss in Chapter 4, Ryden's algorithm seems to converge faster than the Holst-Lindgren algorithm, and has lower computational cost since it does not require the information matrix in the initial phase. We extend Ryden's algorithm to estimate the HBMM parameter online.

2.3 Collaborative spectrum sensing

In radio environments, the detection performance of spectrum sensing is usually compromised by destructive channel conditions with severe shadowing and fading effects, since it is hard to distinguish between an idle spectrum and a weak signal attenuated by deep fading. The consequent hidden terminal effects and other errors can result in harmful interference to PUs. Collaborative or cooperative spectrum sensing techniques leverage multiuser diversity to improve sensing performance. These techniques extend the temporal spectrum sensing method mentioned above by involving multiple SUs in a joint decision-making process to determine when a given channel is idle or active. Collaborative spectrum sensing can be categorized into two main approaches: hard and soft decision schemes.

In hard decision schemes, each SU in a group of SUs makes an independent decision on the active or idle state of the channel. These 1-bit decisions are forwarded to a fusion center, which combines the individual SU decisions into a final decision according to a fusion rule. Two popular fusion rules are the majority vote and the more conservative OR-rule, in which the PU is deemed active if at least one of the SU decides that the PU is

active. Hard decision schemes based on voting among the simplest suboptimal collaboration methods [1]. In soft decision schemes, each of the SUs forwards measurements to the fusion center directly, which combines them linearly according to a set of weights and compares the result to a threshold to determine the final decision. The soft decision scheme proposed in [22] uses the likelihood ratio test (LRT) to implement the Neyman-Pearson classifier. This classifier, however, involves a quadratic form leading to high computation cost, and the performance evaluation and threshold computations are also mathematically less tractable. Soft decision schemes can outperform hard decision schemes in terms of detection accuracy, but the weights for soft fusion must be chosen appropriately, and the computational and communication overhead is much higher.

In [9], a more sophisticated hard decision scheme is studied by taking the sensing throughput and the sensing time into account. In this scheme, by adopting the weighting idea from the soft decision scheme, the 1-bit hard decisions are weighted based on the likelihood ratio test at the fusion sensor. The differences in the reliability of the 1-bit decisions made by different SUs are therefore reflected in the weights of the decisions in the fusion center. However, the global optimum solution for the threshold of the fusion rule and weights for SUs are more difficult to find than in the soft decision scheme. The computational complexity together with its mathematically untractable performance make this scheme less attractive. in [32], a softened hard combination scheme with two-bit overhead for each SU is proposed attempting to make a good tradeoff between the detection accuracy and the communication overhead. However, the weights can only be computed offline. In [44], a simpler detector structure can be used by linearly combining the measurements from the SUs, and a linear fusion rule is proposed for a soft decision scheme. By doing so, the optimal threshold at the fusion center can be jointly determined with the optimal linear combining weights. The weights can be derived using a practical scheme by optimizing the modified deflection coefficient (MDC) which characterizes the probability distribution function of the global test statistic at the fusion center. This approach has less computational

complexity, is more tractable, and achieves performance comparable to the LRT-based fusion. However, all of the aforementioned collaborative spectrum sensing schemes are not model-based. As we will discuss in Chapter 5, the model based collaborative spectrum sensing can provide superior spectrum detection performance.

Chapter 3: Spatial Spectrum Sensing

In this chapter, we focus on the spatial spectrum sensing in cognitive radio network to exploit spectrum holes in the spatial domain. In spatial spectrum sensing, the PU is considered to be active all the time. Thus, SUs cannot transmit in the same frequency band as the PU, unless the SUs move out of the coverage area of the PU. When SUs are sufficiently far away from the PU, the interference caused by SU transmissions can be tolerated by the PU. SUs could efficiently reuse the frequency resource.

Interference analysis plays an important role in spatial spectrum sensing, since it can be used to ensure the performance of the PU, and it can also be used to carry out power control for SUs. Previous research has focused only on interference from a single SU, however, multiple SUs may transmit simultaneously and cause aggregate interference to the PU. In this chapter, we analyze aggregate interference and use this analysis to develop appropriate power control and contention control schemes. The part of the work in this chapter appears in [53].

3.1 System Model

Let us introduce a spatial spectrum sensing model with a single primary transmitter node p, one primary receiver node v (or victim node), and a population of SUs distributed within an area in the Euclidean plane. The point process of SUs is assumed to form a realization of a homogeneous Poisson point process with intensity Λ. Each SU is active with probability α, independent of the other SUs. Using the thinning property of the Poisson point process (see, e.g., [4]), the active SUs form a realization of a homogeneous Poisson point process with intensity $\lambda = \alpha\Lambda$. For an area of interest $\mathbb{A}$, let $\Phi(\mathbb{A})$ denote the number of active SUs in $\mathbb{A}$ and let $|\mathbb{A}|$ denote the physical area corresponding to $\mathbb{A}$. Then the probability
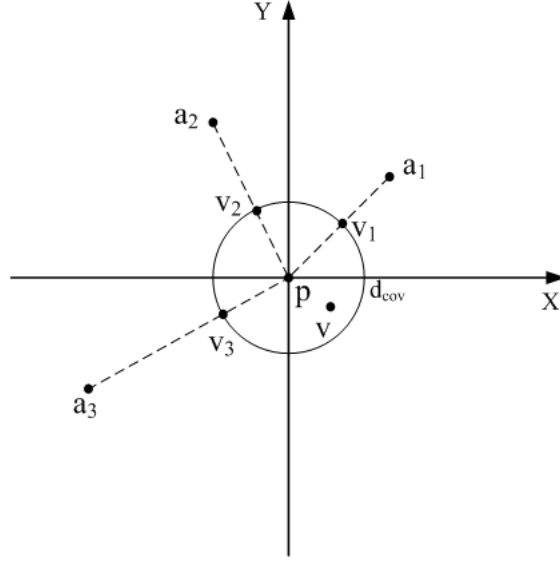
Figure 3.1: Interference scenario.

distribution of $\Phi(\mathbb{A})$ is given by

$$P\{\Phi(\mathbb{A}) = k\} = e^{-\lambda|\mathbb{A}|}\frac{(\lambda|\mathbb{A}|)^k}{k!}, \quad k = 0, 1, 2....\tag{3.1}$$

Let $\mathcal{A} = \{1, \ldots, \Phi(\mathbb{A})\}$ denote the index set of active SUs and let a_i denote the ith SU, $i \in \mathcal{A}$. The system scenario is illustrated in Fig. 3.1. Here, nodes v_1, v_2, and v_3, represent hypothetical victim nodes that lie closest to active SUs a_1, a_2, and a_3, respectively, within the coverage area of p.

We assume that all transmissions are omnidirectional and that signal propagation is governed by a lognormal shadowing model [35, (2.4.15)]. Hence, the propagation loss in dB between two nodes i and j can be expressed as

$$L_{i,j} = g(d_{i,j}, \kappa) + W \quad [\text{dB}],\tag{3.2}$$

where the function $g(d, \kappa)$ represents the path loss component [31]. For simplicity we assume that $g(d, \kappa) = 10\kappa \log_{10} d$ and the path loss factor κ is given, so it can be denoted by $g(d)$.

14

The shadowing noise W is typically modeled as a zero mean white Gaussian noise process with variance σ_w^2, which is independent of the path loss [16]. We denote the Gaussian distribution with mean μ and variance σ^2 by $N(\mu, \sigma^2)$. Thus, $W \sim N(0, \sigma_w^2)$. Hence, the received power at node v due to node p is given by

$$R_v = s_p - L_{p,v} = s_p - g(d_{p,v}) + W \quad \text{[dBm]}, \tag{3.3}$$

where s_p is the transmitted power of node p. Similarly, the received power at node v from node a, where node a is any node chosen from $\mathcal{A} = \{1, \ldots, \Phi(\mathbb{A})\}$, is given by

$$I_v = s_a - L_{a,v} = s_a - g(d_{a,v}) + W \quad \text{[dBm]}, \tag{3.4}$$

where s_a is the transmitted power of node a.

The outage probability of a victim node v with respect to the transmitter p, is the probability that the received power R_v from node p falls below a detection threshold r_{min} [dBm] when p is transmitting (see, e.g. [53] [34]):

$$P_{out}(p, v) \triangleq P\{R_v < r_{min}\}. \tag{3.5}$$

In general, r_{min} is determined by the primary receiver's structure, noise statistics, and quality of service (QoS) requirements. The coverage distance is the maximum distance between the node p and any potential victim node v such that the outage probability does not exceed a threshold $\varepsilon_{cov} > 0$:

$$d_{cov}(p) \triangleq \max\{d_{p,v} : P_{out}(p, v) \leqslant \varepsilon_{cov}\}$$

$$= g^{-1}(s_p - r_{min} + \sigma Q^{-1}(1 - \varepsilon_{cov})), \tag{3.6}$$

where $g^{-1}(\cdot)$ denotes the inverse of $g(\cdot)$ and $Q(x) \triangleq \frac{1}{\sqrt{2\pi}} \int_x^\infty e^{-\frac{t^2}{2}} dt$ denotes the standard Q

function.

The interference probability with respect to a given victim node v is the probability that I_v exceeds an interference tolerance threshold I_{max} [dBm] when node a is transmitting. This threshold can be set to meet the PU's interference tolerance policy as follows:

$$P_{int}(a, v) \triangleq P\{I_v \geqslant I_{max}\}. \tag{3.7}$$

Under the shadowing model, the interference probability is given by

$$P_{int}(a, v) = Q\left(\frac{I_{max} - s_a + g(d_{a,v})}{\sigma_{va}}\right). \tag{3.8}$$

3.2 Aggregate interference

Based on the above system model, we analyze the aggregate interference for a cognitive radio network represented in a Euclidean plane. In the Euclidean plane, the norm for a position vector $z = (z_1, z_2)$ is given by $\|z\| = \sqrt{z_1^2 + z_2^2}$. The scenario is shown in Fig. 3.1, with the primary transmitter located in the center of the plane.

We assume that all SUs employ a Listen-Before-Talk (LBT) scheme [28, 29] to dynamically access the available spectrum. In the LBT scheme, each SU consists of two states: listen state and talk state. During the listen state, the SU does not transmit any signal, but it estimates the power of the received signal from the primary transmitter to determine whether it can switch to the talk state to transmit a signal. For example, if the received power $R < \eta$, the SU would switch to the talk state; otherwise, it remains in the listen state. During the talk state, the SU can transmit at a fixed power. After transmitting for a pre-specified maximum duration, it returns to the listen state to listen again. Compared with other models, which depend on the primary receivers to send out beacons to notify other nodes of their locations [41], the LBT model requires less energy and fewer bandwidth resources.

In the LBT scheme, each of the active SU a_i, $i \in \mathcal{A}$, compares the received power from the primary transmitter to a deterministic threshold η. We introduce a function $U(x)$ to indicate whether a SU located at position x in the Euclidean plane has the right to access the network:

$$U(x) = \begin{cases} 1, & s_p - g(\|x\|) + W_{pa} < \eta, \\ 0, & \text{otherwise,} \end{cases} \tag{3.9}$$

where $W_{pa} \sim N(0, \sigma_{pa}^2)$ is the shadowing noise between the primary transmitter and SU. If $U(x) = 1$, it means this SU located at position x is sufficiently far away from the primary transmitter, therefore it can transmit with the same frequency band as the primary transmitter.

At the first place, we assume that each SU a_i, $i \in \mathcal{A}$, transmits with a fixed power s_a if it has the right to access network. Let x_i denote the position vector corresponding to the SU a_i, $i \in \mathcal{A}$. The shadowing noise received at the victim node v due to the transmission of SU is given by $W_{va} \sim N(0, \sigma_{va}^2)$. Hence, given the location of the primary receiver x_v, the aggregate interference from SUs can be characterized as

$$I = \sum_{i \in \mathcal{A}} U(x_i) \cdot 10^{\frac{s_a - g(\|x_i - x_v\|) + W_{va}}{10}} = \sum_{i \in \mathcal{A}} U(x_i) h(x_i) 10^{\frac{W_{va}}{10}}, \tag{3.10}$$

where the summation is over the index set of SUs a_i, $i \in \mathcal{A}$, and

$$h(x) = 10^{\frac{s_a - g(\|x - x_v\|)}{10}}.$$

Here, the aggregate interference is given in linear scale. Given the location information Ω of all SUs, the moment generating function (see, e.g., [23, Chap. 8]) of the aggregate

interference can be derived as follows:

$$M_I(t) = E[e^{tI}] = E\left[e^{t\sum_{i\in\mathcal{A}} U(x_i)h(x_i)10^{\frac{W_{va}}{10}}}\right]$$

$$= \prod_{i\in\mathcal{A}} E\left[e^{tU(x_i)h(x_i)10^{\frac{W_{va}}{10}}}\right]$$

$$= E\left[\prod_{i\in\mathcal{A}} E\left[e^{tU(x_i)h(x_i)10^{\frac{W_{va}}{10}}}\;\middle|\;\Omega\right]\right]. \tag{3.11}$$

Suppose $\{x_i\}$ is a Poisson point process with intensity measure $m(x)dx$. Using properties of the Laplace functional of the Poisson point process [4], [51], we can obtain the following equation for all nonnegative functions $v(x)$ satisfying $\int_{R^2}(1-v(x))m(x)dx < \infty$:

$$E\left[\prod_{i\in\mathcal{A}} v(x_i)\right] = \exp\left\{-\int_{\mathbb{R}^2}(1-v(x))m(x)dx\right\}. \tag{3.12}$$

Let

$$v(x) = E\left[e^{tU(x)h(x)10^{\frac{W_{va}}{10}}}\;\middle|\;\Omega\right]. \tag{3.13}$$

Applying (3.12) and (3.13) into (3.11), we can obtain the following alternative expression for $M_I(t)$:

$$M_I(t) = \exp\left\{-\lambda\int_{\mathbb{R}^2}\left(1 - E\left[e^{tU(x)h(x)10^{\frac{W_{va}}{10}}}\;\middle|\;\Omega\right]\right)dx\right\}. \tag{3.14}$$

From the moment generating function, we can obtain the expectation of the aggregate interference. The shadowing noise variables W_{pa} and W_{va} are independent of each other, and are independent of the locations of SUs. For simplicity, W_{pa} is determined by the primary transmitter and W_{va} is determined by the victim receiver.

From the moment generating function $M_I(t)$, the expectation of the aggregate interference can be obtained as follows:

$$E(I) = \frac{dM_I(t)}{dt}\Big|_{t=0}$$

$$= \lambda \int_{\mathbb{R}^2} E\left[U(x)h(x)10^{\frac{W_{va}}{10}}\,\Big|\,\Omega\right]dx$$

$$= \lambda \int_{\mathbb{R}^2} h(x)E[U(x)\mid\Omega]\cdot E\left[10^{\frac{W_{va}}{10}}\right]dx. \tag{3.15}$$

Here,

$$E\left[10^{\frac{W_{va}}{10}}\right] = \int_{-\infty}^{+\infty} 10^{\frac{w}{10}}\cdot f(w;\sigma_{va}^2)dw = e^{\omega_{va}}, \tag{3.16}$$

where $\omega_{va} \triangleq \frac{\sigma_{va}^2}{2(10\log_{10}e)^2}$ and $f(w;\sigma_{va}^2)$ denotes the probability density function (pdf) of W_{va}, and

$$E[U(x)\mid\Omega] = \int_{-\infty}^{\eta-s_p+g(\|x\|)} f(w;\sigma_{pa}^2)dw = \beta(x), \tag{3.17}$$

where $\beta(x) \triangleq 1 - Q(\frac{\eta-s_p+g(\|x\|)}{\sigma_{pa}})$ and $f(w;\sigma_{pa}^2)$ denotes the pdf of W_{pa}. Using (3.15)–(3.17) we have

$$E[I] = \lambda e^{\omega_{va}} F(s_a, x_v), \tag{3.18}$$

with

$$F(s_a, x_v) = \int_{\mathbb{R}^2} \beta(x)h(x)dx.$$

From the moment generating function, we can also obtain the cumulant generating function $G(t) = \ln M_I(t)$, which is just the logarithm of the moment generating function $M_I(t)$. Then the cumulants can be obtained from the power expansion of the cumulant generating

19

function. The nth order cumulant $\tilde{\kappa}_n$ is given as:

$$\tilde{\kappa}_n = \frac{\partial^n}{\partial t^n} G(t) \Big|_{t=0}$$

$$= \lambda e^{n^2 \omega_{va}} \int_{\mathbb{R}^2} \beta(x) h^n(x) dx. \tag{3.19}$$

Although a closed-form of the probability density function for the aggregate interference cannot be found, it has been shown in [48], [14] that the lognormal distribution can be used to approximate the probability density function of the aggregate interference, when the uniform distributed interferers are at a specified minimum distance (protection distance) from the primary transmitter.

The probability density function of a lognormal variable y is

$$p(y) = \frac{1}{\sqrt{2\pi}\sigma y} \exp\left(\frac{-(\ln(y) - \mu)^2}{2\sigma^2}\right), \tag{3.20}$$

If the lognormal distribution is used to approximate the distribution of the aggregate interference, the mean and variance can be estimated using its first order cumulant $\tilde{\kappa}_1$ and second order cumulant $\tilde{\kappa}_2$ as follows:

$$\mu = \ln\left(\frac{\tilde{\kappa}_1^2}{\sqrt{\tilde{\kappa}_2 + \tilde{\kappa}_1^2}}\right), \sigma = \sqrt{\ln\left(\frac{\tilde{\kappa}_2}{\tilde{\kappa}_1^2} + 1\right)}. \tag{3.21}$$

3.3 Power Control based on Aggregate Interference

Instead of choosing fixed power for all SUs, it is more appropriate for each SU to carry out power control and transmit with its own power, since the distances between different SUs and primary receiver are different. Intuitively, the closer the distance between the SU and the primary receiver, the smaller the transmission power should be in order to avoid excessive interference inflicted on the primary receiver. As described in [34], for a single

SU, the maximum interference-free transmit power (MIFTP) can be defined in terms of the worst-case interference probability:

$$P_{int}(a) = \sup_v P_{int}(a, v) = Q\left(\frac{I_{max} - s_a + g(d_a^*)}{\sigma_{va}}\right), \qquad (3.22)$$

where $d_a^* \triangleq d_{p,a} - d_{cov}(p)$ is called the critical distance for the SU a with respect to the primary transmitter p, and the supremum is taken over all potential victim nodes v such that $d_{p,v} \leq d_{cov}(p)$. The MIFTP is then given by $s_a^* = \max\{s_a : P_{int}(a) \leq \varepsilon_{int}\}$, and we have

$$s_a^* = \begin{cases} I_{max} + g(d_a^*) - \sigma_{va}Q^{-1}(\varepsilon_{int}), & \text{if } d_{p,a} > d_{cov}(p), \\ -\infty, & \text{otherwise.} \end{cases} \qquad (3.23)$$

However, in the system model presented above, multiple SUs may transmit signals at the same time. The critical distance for the ith SU is defined as $d_{a_i}^* \triangleq d_{p,a_i} - d_{cov}(p) = \|x_i\| - d_{cov}$. In Fig. 3.1, the critical distances corresponding to the SUs a_1, a_2, and a_3, are given by d_{a_1,v_1}, d_{a_2,v_2}, and d_{a_3,v_3}, respectively. We assume that each SU that has the right to access the network can contribute at most i_{max} interference to the victim node v, such that the sum of i_{max} over all such SUs should satisfy $\sum_{i\in\mathcal{A}} U(x_i)i_{max} \leq I_{max}$. Then the ith SU is permitted to transmit at a power level not exceeding its *group* MIFTP or G-MIFTP defined as follows:

$$s_{a_i}^* = \begin{cases} i_{max} + g(d_{a_i}^*) - \sigma_{va}Q^{-1}(\varepsilon_{int}), & \text{if } d_{p,a_i} > d_{cov}(p), \\ -\infty, & \text{otherwise.} \end{cases} \qquad (3.24)$$

Therefore, the goal to obtain the G-MIFTP for SUs can be accomplished by selecting an appropriate value for i_{max}. If each SU that has permission to access the network can transmit with G-MIFTP, then the moment generating function of the aggregate interference can be derived similarly as in the fixed transmission power case. The expectation of the

21

aggregate interference can be derived from the moment generating function and is given by

$$E[I] = \lambda e^{\omega_{va}} \cdot \psi(i_{max}) F(x_v), \tag{3.25}$$

with

$$F(x_v) = \int_{\mathbb{R}^2} \beta(x) 10^{\frac{g(\|x\|-d_{cov})-g(\|x-x_v\|)}{10}} dx$$

$$= \int_{\mathbb{R}^2} \beta(x) \left(\frac{\|x\| - d_{cov}}{\|x - x_v\|} \right)^{\kappa} dx,$$

and

$$\psi(i_{max}) = 10^{\frac{i_{max} - \sigma_{va} Q^{-1}(\varepsilon_{int})}{10}}. \tag{3.26}$$

From the moment generating function of the aggregate interference, we can also obtain the variance of the aggregate interference and is given by

$$\mathrm{Var}(I) = \lambda e^{\frac{\omega_{va}}{4}} \cdot \psi^2(i_{max}) \Gamma(x_v), \tag{3.27}$$

with

$$\Gamma(x_v) = \int_{\mathbb{R}^2} \beta(x) 10^{\frac{g(\|x\|-d_{cov})-g(\|x-x_v\|)}{5}} dx$$

$$= \int_{\mathbb{R}^2} \beta(x) \left(\frac{\|x\| - d_{cov}}{\|x - x_v\|} \right)^{2\kappa} dx.$$

When all SUs are carrying out power control with G-MIFTP, The distribution of the aggregate interference can also be approximated by the lognormal distribution, and cumulants are given by

$$\tilde{\kappa}_n = \lambda e^{n^2 \omega_{va}} \cdot \psi^n(i_{max}) \int_{\mathbb{R}^2} \beta(x) \left(\frac{\|x\| - d_{cov}}{\|x - x_v\|} \right)^{n\kappa} dx. \tag{3.28}$$

With cumulants, the probability density function of the aggregate interference can also be

obtained, which would be an expression containing the variable i_{max}. Similar with power control using MIFTP, the probability that the aggregate interference exceeding the threshold I_{max} should be less than ε_{int}, so the following condition should be satisfied

$$P(I \geq I_{max}) \leq \varepsilon_{int}. \tag{3.29}$$

Using the approximated distribution of the aggregate interference together with the inequality (3.29), i_{max} can be determined, thus each active SU can transmit with power up to its own G-MIFTP given by (3.24).

3.4   Hybrid Power/Contention Control

Power control let SUs transmit simultaneously without causing harmful interference to the PU. However, collisions between SUs may still occur when one SU is located very close to its neighbor SU. Even though SUs are granted the right to access the spectrum resource of the PU, interference between SUs can also lead to transmission failure. The multiple access scheme in the MAC layer can address this issue by implementing contention control among SUs, and carrier sense multiple access with collision avoidance (CSMA/CA) is widely used in wireless networks.

If the SUs employ CSMA/CA, then each SU would sense the medium before its transmission. If the medium is busy, an active SU defers its transmission with a random backoff time. Otherwise, the SU gets the opportunity to access the medium. Assume the ith SU is transmitting with power s_{a_i}, and R_{a_j} indicates the received power at the jth SU which is sensing the medium at distance d_{a_i,a_j} away from the ith SU. Then the received power R_{a_j}, which is viewed as interference, to the jth SU can be expressed as

$$R_{a_j} = s_{a_i} - g(d_{a_i,a_j}) + W_a \quad \text{[dBm]}, \tag{3.30}$$

where $W_a \sim N(0, \sigma_a^2)$ is the shadowing noise between the SUs. The medium is determined

to be busy to the jth SU if R_{a_j} is larger than a threshold η_{det}. Based on that, we can define the detection probability:

$$P_{det} \triangleq P\{R_{a_j} \geq \eta_{det}\}. \tag{3.31}$$

As a result of contention control with CSMA/CA, all SUs are separated from each other by at least a contention distance away. Given a threshold ε_{det}, the contention distance d_{min} can be defined as

$$d_{min} \triangleq \min\{d_a : P_{det} \leq \varepsilon_{det}\}. \tag{3.32}$$

As shown in [17], if all SUs transmit with fixed power and apply CSMA/CA, then the distribution of the active SUs can be modeled as Matern-Hardcore (MH) point process. An MH point process is a dependent thinning process from the original Poisson point process, which means that the point positions are correlated to each other. In the MH point process, a random mark is associated with each point, and a point is deleted from the original point process if there exists another point within distance d_{min} with a smaller marker. The retaining probability q_{mh} for the MH point process, which is the probability of a point from a Poisson point process with a density λ surviving the thinning process, is given by

$$q_{mh} = \frac{1 - e^{-\lambda \pi d_{min}^2}}{\lambda \pi d_{min}^2}. \tag{3.33}$$

However, it is very difficult to analyze the distribution of aggregate interference with the MH point process. In [7], an independent thinned Poisson point process is used to approximate the MH point process to carry out the aggregate interference analysis. The intensity of this independent thinned Poisson point process, denoted by λ_{mh}, is given by

$$\lambda_{mh} = \lambda \cdot q_{mh}. \tag{3.34}$$

As shown in [7], when SUs are transmitting with fixed power, the lognormal fitting for the aggregate interference distribution with the independent thinned Poisson point process

approximation is fairly accurate compared to simulation result with the MH point process. Thus, for aggregate interference analysis, the MH point process can be replaced by an independent thinned Poisson point process with intensity λ_{mh}.

It would be preferable to combine contention control with power control. A hybrid scheme can be carried out in the following manner: First contention control is applied, resulting in a set of active SUs following an MH point process. Then, power control is employed to adjust the transmission power for each active SU allowing them to transmit with G-MIFTP.

The remaining issue is how to determine an initial fixed power s_a and the contention distance d_{min} for the MH process in the contention control step. The initial power s_a and the contention distance d_{min} should satisfy certain conditions in order to ensure that the detection threshold P_{det} between two active SUs is less than ε_{det} even after the power control step. Basically, the initial fixed power s_a for all of SUs should be large enough, and consequently a large enough d_{min} can be determined.

A conservative method to determine the initial fixed power s_a is to use an MIFTP power control scheme. According to the MIFTP power control scheme in (3.23), the SU has the maximum MIFTP when the distance d_a^* is maximum. In other words, the SU at the location with the largest d_a^* distance has larger transmission power than at any other location in the Euclidean plane. Moreover, this maximum MIFTP is larger than any specific transmission power in the G-MIFTP power control scheme when multiple SUs are allowed to transmit. If we assume all of the SUs are scattered inside a disc with radius r, then this maximum MIFTP can be achieved at the edge of the disc with $d_{max}^* = r - d_{cov}(p)$, and the value of this maximum MIFTP can be determined by

$$s_{max}^* \triangleq I_{max} + g(d_{max}^*) - \sigma_{va}Q^{-1}(\varepsilon_{int}). \tag{3.35}$$

Subsequently, the contention distance d_{min} can be obtained by substituting s_{max}^* into the
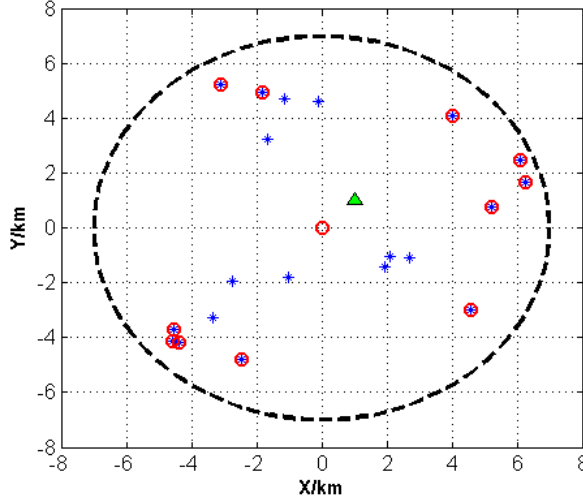
Figure 3.2: Simulation scenario.

following equation which is derived from (3.30)-(3.32):

$$d_{min} = g^{-1}(s_{max}^* - \eta_{det} + \sigma_a Q^{-1}(\varepsilon_{det})). \tag{3.36}$$

Then, G-MIFTP power control is carried out to let each SU transmit with G-MIFTP. Because the aggregate interference analysis for MH point process is approximated by the independent thinned Poisson point process with intensity λ_{mh}, the mean and variance of the aggregate interference, together with the cumulants for the probability density function can be calculated the same way as we did in (3.25),(3.27),(3.28). Then the G-MIFTP for each SU in the MH point process, can be obtained using (3.24). Consequently, the proposed hybrid contention and power control scheme can satisfy the performance requirement for both the PUs and SUs.

3.5 Numerical Results

In this section, we present numerical results to demonstrate the accuracy of our aggregate interference analysis and the performance of our proposed power control and contention
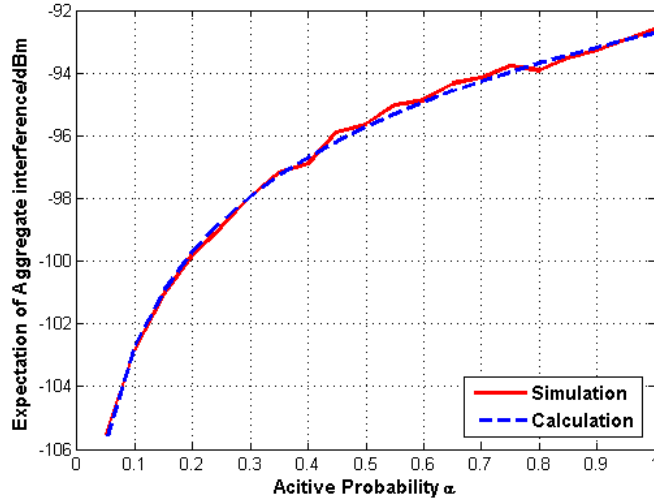
26

Figure 3.3: Expectation of aggregate interference for fixed power s_a.

control scheme. The simulation scenario is shown in Fig. 3.2. The area of interest is a disk with radius $r = 7$ km, which is illustrated by a dashed circle. The primary transmitter denoted by a small red circle is located at the center of the Euclidean plane (0,0) km, and the primary receiver denoted by a green triangle is located at (1,1) km. The blue stars represent all SUs having the right to transmit in the area, and the blue stars enclosed in small red circles represent the SUs that are actually transmitting with the same frequency band as the primary transmitter at this moment.

3.5.1 Fixed transmission power s_a

In this case, we assume each SU transmits at a fix power level $s_a = 40$ dBm, the transmission power for the primary transmitter $s_p = 40$ dBm, Listen-Before-Talk threshold $\eta = -110$ dBm, path loss factor $\kappa = 4$, and shadowing loss parameters $\sigma_{va} = 2$ dB, $\sigma_{pa} = 2$ dB. The intensity of the Poisson point process is given by $\Lambda = 1.0 \times 10^{-6}$, while the active probability α is a parameter that is varied in our simulation ranging from 0.1 to 1.0.

With the above parameter values, we ran simulations to get the aggregate interference
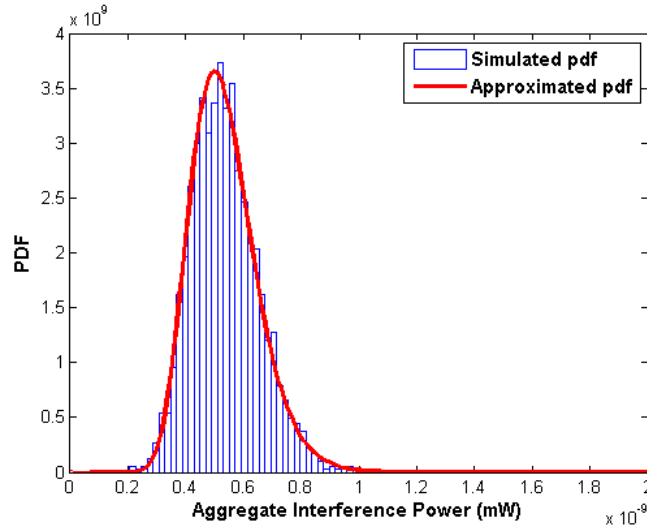
Figure 3.4: Lognormal approximation of the aggregate interference for fixed power.

to the primary receiver. The simulated aggregate interference was averaged over 2000 iterations and shown in Fig. 3.3. On the other hand, we can also theoretically calculate the expectation of the aggregate interference with (3.18). Fig. 3.3 shows that the theoretical result matches the simulation result very well. In addition, when the active probability α increases, the number of transmitting SUs increases correspondingly, and the expectation of the aggregate interference also increases.

In addition, simulations were performed to verify that the distribution of the aggregate interference can be well approximated by the lognormal distribution. With the parameter setting given above, and the active probability α fixed at 1.0, we repeated the simulation 2000 times. We then plotted the probability density function of the aggregate interference in Fig. 3.4. In addition, we calculated cumulants for the aggregate interference with (3.19), from which the mean and variance for the lognormal distribution can be calculated using (3.21), which gave values of $\mu = -21.3712$ and $\sigma = 0.2134$.

Fig. 3.4 shows that the simulated probability density function matches the lognormal distribution very well. This numerically justifies use of the lognormal distribution to approximate the aggregate interference when SUs are transmitting with fixed power.
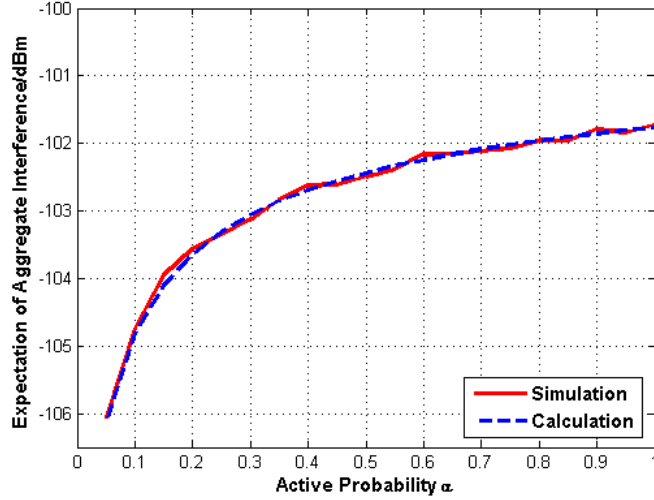
28

Figure 3.5: Expectation of aggregate interference for G-MIFTP model.

3.5.2 Transmission with G-MIFTP

In this case, we let each active SU transmits with its own G-MIFTP. Parameters are given as follows: transmission power for the primary transmitter $s_p = 40$ dBm, Listen-Before-Talk threshold $\eta = -110$ dBm, path loss factor $\kappa = 4$, shadowing loss parameters $\sigma_{va} = 2$ dB, $\sigma_{pa} = 2$ dB, $\varepsilon_{int} = 0.01$, $\varepsilon_{cov} = 0.05$, detection threshold $r_{min} = -90$ dBm, and aggregate interference threshold $I_{max} = -100$ dBm. The intensity of the Poisson point process is given by $\Lambda = 1.0 \times 10^{-6}$, while the active probability α is a parameter that is varied in our simulation ranging from 0.1 to 1.0.

Simulations were performed to analyze the aggregate interference to the primary receiver. If we fixed the active probability $\alpha = 1.0$, when SUs transmit with G-MIFTP, the distribution of the aggregate interference can be approximated by the lognormal distribution with $\mu = -23.4492$ and $\sigma = 0.1820$ calculated from cumulants in (3.28), which is verified in Fig. 3.6.

With the approximated lognormal distribution, we carried out G-MIFTP power control for SUs based on (3.29). According to our system requirement, the aggregate interference should exceed the threshold I_{max} with probability less than $\varepsilon_{int} = 0.01$. During our 3000
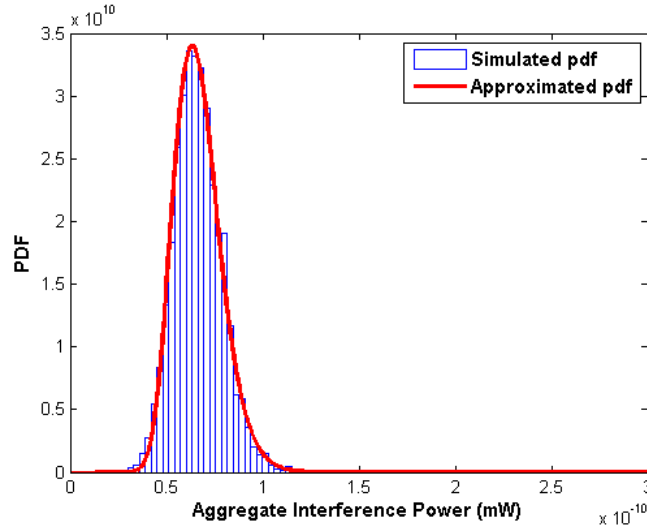
Figure 3.6: Lognormal approximation of the aggregate interference for G-MIFTP.

iterations, there are only 22 times that the aggregate interference would exceed the threshold I_{max}. In addition, Fig. 3.5 shows that the expectation of the aggregate interference calculated with (3.25) matches the averaged simulation result very well. Meanwhile, the expectation of the aggregate interference can be always maintained under the threshold $I_{max} = -100$ dBm. Thus, the proposed G-MIFTP power control scheme can let each SU transmit with its own G-MIFTP without causing harmful interference to the primary receiver.

3.5.3 Hybrid power/contention control

We also ran simulations to evaluate the hybrid contention and power control scheme. Parameters are given as follows: transmission power for the primary transmitter $s_p = 40$ dBm, Listen-Before-Talk threshold $\eta = -110$ dBm, path loss factor $\kappa = 4$, shadowing loss parameters $\sigma_{va} = 2$ dB, $\sigma_{pa} = 2$ dB, $\sigma_a = 2$ dB, $\varepsilon_{int} = 0.01$, $\varepsilon_{cov} = 0.05$, detection threshold $r_{min} = -90$ dBm, and aggregate interference threshold $I_{max} = -100$ dBm. In addition, the detection threshold $\eta_{det} = -80$dBm and the detection probability $P_{det} = 0.01$. The intensity of the Poisson point process is given by $\Lambda = 1.0 \times 10^{-6}$, while the active probability α
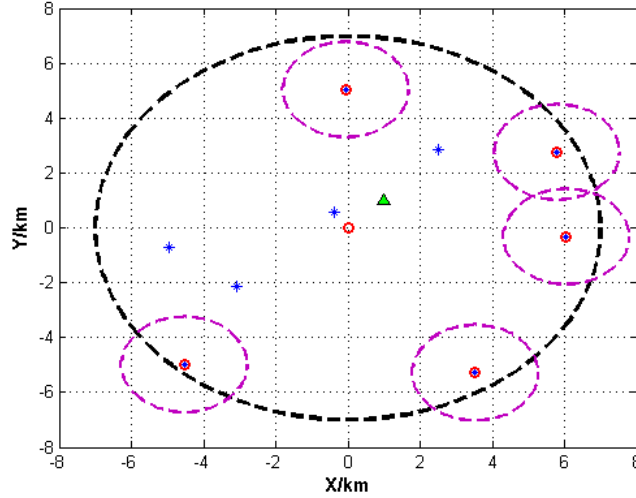
Figure 3.7: Simulation scenario for contention/power control.

is a parameter that is varied in our simulation ranging from 0.1 to 1.0.

Contention control between SUs was first carried out with the maximum MIFTP s^*_{max} calculated from (3.35). As a result of contention control, the distance between any two active SUs is at least $d_{min} = 1.748$ km away, and it is illustrated by red dashed circles as shown in Fig. 3.7.

Each SU carries out power control to transmit with its own G-MIFTP. According to our system requirement, after the power control, the aggregate interference should exceed threshold I_{max} with probability less than $\varepsilon_{int} = 0.01$. In 3000 iterations, there were only 5 times that the aggregate interference exceeded the threshold I_{max}. In addition, Fig. 3.8 shows that the expectation of the aggregate interference matches the simulation result very well, and the expectation of the aggregate interference is always lower than $I_{max} = -100$ dBm. So our hybrid contention and power control scheme can allow multiple simultaneous spectrum access for SUs and also take the aggregate interference to the PU into account.

Finally, we compare the achievable overall capacity between the MIFTP power control scheme [34] and our hybrid power/contention control scheme. In the MIFTP power control

31
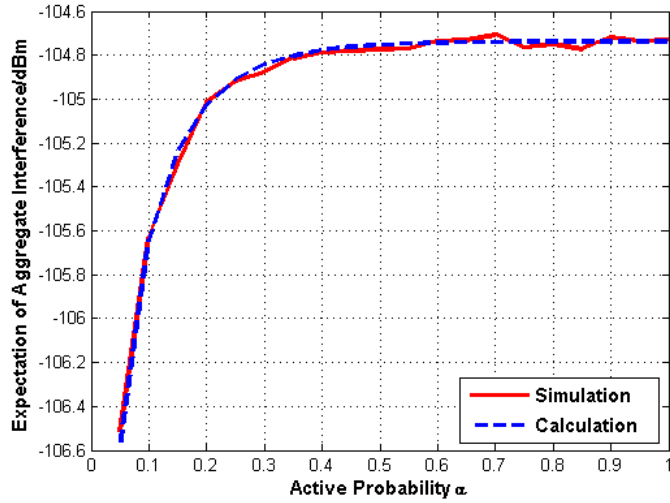
Figure 3.8: Expectation of aggregate interference for contention/power control.
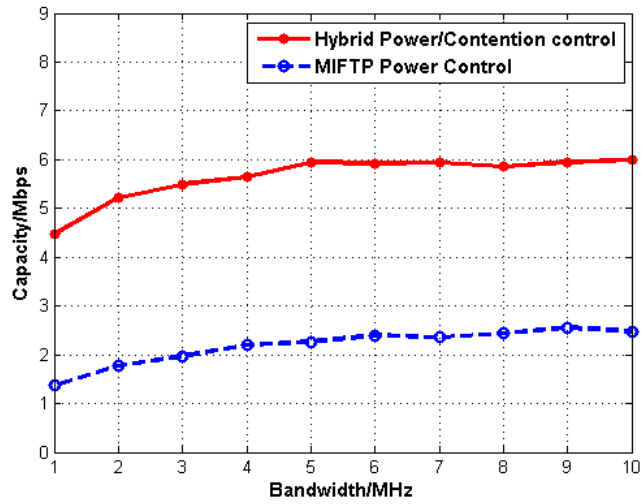
Figure 3.9: Overall capacity comparison at $\alpha = 1$.

scheme, only one secondary transmitter-receiver pair is allowed to communicate, but in the hybrid power/contention control scheme more than one pair may transmit simultaneously. So we define the overall capacity for the hybrid power/contention control as the summation of the capacities from each secondary transmission pair. With (3.24), the achievable capacity for the ith secondary transmitter-receiver pair is given by:

$$C_i = B \cdot E \left\{ \log_2 \left(1 + \frac{R_i}{N_0 B} \right) \right\}$$

$$= B \cdot E \left\{ \log_2 \left(1 + \frac{(d_i/d_0)^{-\kappa}}{N_0 B} \cdot 10^{(s_{a_i}^* + W)/10} \right) \right\}, \qquad (3.37)$$

where R_i denotes the receiver power at the ith secondary receiver, the expectation $E[\cdot]$ is taken with respect to the shadowing noise W, and the transmitter-receiver distance is d_i. In the simulation, we set $d_i = 1$ km and $d_0 = 1$ m. The power spectral density $N_0 = -137$dBm/Hz, and the bandwidth B varies from 1M to 10M. By comparing the overall capacity, Fig. 3.9 shows that the hybrid power/contention control scheme outperforms the MIFTP power control scheme, since multiple SUs are allowed to transmit at the same time without causing harmful interference between each other and to the PU.

Chapter 4: Temporal Spectrum Sensing

In this chapter, we focus on temporal spectrum sensing in cognitive radio networks, which exploits spectrum holes in the time domain. In temporal spectrum sensing, the primary system is not active all the time, so SUs can transmit with the licensed spectrum resource when primary system is idle. SUs have the responsibility to monitor the state of the primary system. If the primary transmitter is idle, SUs must be able to detect the availability of the spectrum resource and make decision to access. If the primary transmitter becomes active again, SUs must vacate current spectrum resource and search for another available spectrum resource.

The HBMM has the capability to model the channel occupancy behavior of primary system [40], and given the HBMM parameter we are able to perform better dynamic spectrum access. In this chapter, we start by discussing the HBMM and its application to spectrum sensing. In addition, we briefly review online parameter estimation for HMMs. Then we propose our online parameter estimation algorithm for HBMM and evaluate its performance. The work in this chapter appears in [54].

4.1 Temporal spectrum sensing based on a HBMM

4.1.1 System model

In temporal spectrum sensing, the PU alternates between an active state, in which a signal of fixed output power is transmitted over a narrowband channel and an idle state, in which no signal is transmitted. The wireless propagation environment is assumed to be governed by a standard path loss with lognormal shadowing model. For a receiver at a distance δ from the PU, the overall log-distance path loss with shadowing, measured in dB, is given

by [35, pp. 40-41]

$$L_p(\delta) = \bar{L}_p(\delta_0) + 10\kappa \log_{10}\left(\frac{\delta}{\delta_0}\right) + \epsilon_{\mathrm{dB}}, \quad \delta \geq \delta_0, \tag{4.1}$$

where δ_0 denotes the close-in reference distance, $\bar{L}_p(\delta_0)$ is the average log-distance path loss at the reference distance δ_0, κ is the path loss exponent, and ϵ_{dB} is the shadowing noise, which is assumed to be a Gaussian random variable with zero mean and variance σ_ϵ^2. We ignore fast fading since it can be reduced effectively by an averaging filter (cf. [33]).

We shall assume a discrete-time model. Let Y_k denote the received signal power at time k from the PU, measured in units of dBm, by the cognitive radio. Let X_k denote the transmission state of the PU at time k. We use $X_k = 1$ to signify the idle state, i.e., no transmission by the PU and $X_k = 2$ to indicate the active state, i.e., transmission by the PU. Under the path loss model in (4.1), Y_k depends on X_k as follows:

$$Y_k = \begin{cases} \mu_1 + \epsilon_{1,\mathrm{dB}}, & X_k = 1, \\ \mu_2 + \epsilon_{2,\mathrm{dB}}, & X_k = 2, \end{cases} \tag{4.2}$$

where μ_a represents the mean received signal power in dBm and $\epsilon_{a,\mathrm{dB}}$ is a zero-mean Gaussian random variable with variance σ_a^2 representing the associated shadowing noise, when the transmission state of the PU is $a \in \{1, 2\}$. The signal power μ_a results from the transmit power in state a and the path loss from transmitter to receiver, as expressed in the deterministic part of (4.1).

Typically, the sequence Y of received signal powers undergoes pre-processing at the front-end of the receiver. For example, usually some form of averaging is applied to the received signal power samples to diminish the effect of fast fading in the wireless propagation environment (cf. [33]). After applying averaging, the front-end becomes essentially the same as that of a classical energy detector. With a slight abuse of notation, we shall refer to the output of the receiver front-end as $Y = \{Y_k\}_{k=1}^\infty$. In this case, the form of relation (4.2)

remains valid, i.e., Y is conditionally Gaussian given X.

4.1.2 Hidden bivariate Markov model

In the literature on spectrum sensing, the PU state sequence X is commonly assumed to be a Markov chain (cf. [2, 13, 15, 18, 39, 56]). In this case, the joint process (Y, X) is an HMM (see, e.g., [11] for a review of HMMs). HMMs have been applied as models for a cognitive radio channel in several papers, e.g., [2, 18, 39, 56]. A limitation of the HMM, however, is that the Markov assumption on the state sequence X restricts the sojourn time in a given state to be geometrically distributed. On the other hand, empirical studies have shown that the state sojourn time distributions are often not adequately characterized by geometric distributions. For example, in [13], a continuous-time semi-Markov process was proposed as a model for the state process, while in [57], source traffic models with lognormal and extreme value sojourn time distributions were studied.

The HBMM adopted in this thesis is a trivariate process (Y, X, S), where Y denotes an observable process with continuous alphabet and the underlying sequence, $Z = (X, S)$, is a finite state bivariate Markov chain. In this setup, the auxiliary process S, together with the PU state process X, form a Markov chain, such that X alone is not Markov, and consequently, its sojourn time in each state has a phase-type distribution. Such distribution is far more general than the geometric distribution of the HMM, as we elaborate below. For a general HBMM, we denote the state-space of X by $\mathbb{X} = \{1, \ldots, d\}$ and the state-space of S by $\mathbb{S} = \{1, \ldots, r\}$. The state-space of Z is given by $\mathbb{Z} = \mathbb{X} \times \mathbb{S}$. The processes Y and S are assumed to be conditionally independent given X. In addition, Y given X is a sequence of independent, identically distributed (iid) random variables.

Let $f(y; \theta_a)$ denote the conditional density of Y_k given $X_k = a$, where θ_a is a parameter depending on $a \in \mathbb{X}$. In the spectrum sensing application, the form of $f(y; \theta_a)$ depends on the particular channel model and receiver front-end assumed. Under the setup of (4.2), $f(y; \theta_a)$ is a Gaussian density and in this case, we set $\theta_a = (\mu_a, \sigma_a)$, where μ_a and σ_a denote the mean and standard deviation in state a. The d-tuple $\theta = (\theta_a : a \in \mathbb{X})$ specifies

the conditional Gaussian parameters of the HBMM. Different channel models and receiver front-ends could be accommodated within the HBMM framework by modifying the form of $f(y; \theta_a)$ appropriately. We remark that the assumption that Y is conditionally independent given X could be relaxed by characterizing the observable process as a vector process $\mathbf{Y} = \{\mathbf{Y}_n\}$, where the random vector $\mathbf{Y}_n$ captures correlations among consecutive components of the process Y. For example, to capture pairwise correlations in the observable process, one could define $\mathbf{Y}_n = (Y_{2n-1}, Y_{2n})$, $n = 1, 2, \ldots$. Nevertheless, the simple Gaussian-based HBMM was found to be quite accurate in modeling real spectrum measurement data [38,40].

Let P denote the underlying probability measure. The initial distribution of the bivariate Markov chain Z is denoted by the $1 \times dr$ row vector $\pi = [\pi_{(a,i)} : (a, i) \in \mathbb{Z}]$, where $\pi_{(a,i)} = P(Z_1 = (a, i))$, and lexicographic ordering of the bivariate states is assumed. The transition probability matrix of Z is denoted by the $dr \times dr$ matrix $G = [g_{ab}(ij) : (a, i), (b, j) \in \mathbb{Z}]$, where $g_{ab}(ij) = P(Z_2 = (b, j) \mid Z_1 = (a, i))$. The transition matrix can be expressed as a block matrix $G = [G_{ab} : a, b \in \mathbb{X}]$, where $G_{ab} = [g_{ab}(i, j) : i, j \in \mathbb{S}]$ is an $r \times r$ matrix.

Statistical properties of discrete-time bivariate Markov chains are discussed in [40], [10, Chapter 8]. In particular, the sojourn time of the process X in each state $a \in \mathbb{X}$ has a discrete-time phase-type distribution. Suppose that X jumps at some time k. Let ζ_a denote the conditional distribution of S_k given that $X_k = a$. Then the probability mass function of the sojourn time of X in state a is given by

$$p(t \mid a) = \zeta_a G_{aa}^{t-1}(I - G_{aa})\mathbf{1}, \quad t = 1, 2, \ldots, \tag{4.3}$$

where $\mathbf{1}$ denotes a column vector of all ones and I denotes an identity matrix of a given dimension. This is a discrete phase-type distribution with parameter (ζ_a, G_{aa}) [37, p. 46]. The family of phase-type distributions is dense in the set of distributions on $\{0, 1, 2, \ldots\}$ [26, p. 54] and includes convolutions as well as mixtures of geometric distributions. Thus, a phase-type distribution can approximate any given state sojourn time distribution arbitrarily closely. Increasing the number of states of the process S allows more degrees of freedom

in the phase-type sojourn time distribution.

The parameter of the HBMM is specified by $\phi = (\pi, \theta, G)$. We note that the number of elements in the parameter ϕ could be reduced, since each row of G sums to one. However, there is a practical benefit to retaining the entire matrix G as part of the HBMM parameter (see Section 4.3.1). When an HMM (Y, X) is used instead of the HBMM, Y given X is assumed to have the same distribution as in the HBMM. The initial distribution π is given by the $1 \times d$ vector $\pi = [\pi_a : a \in \mathbb{X}]$ with $\pi_a = P(X_1 = a)$, and the transition matrix G is given by $G = [g_{ab} : a, b \in \mathbb{X}]$, where $g_{ab} = P(X_2 = b \mid X_1 = a)$. Clearly, the HMM parameter represents a special HBMM for which $r = 1$.

4.1.3   State and parameter estimation

In the spectrum sensing approach developed in [40], a training sequence of signal strength measurements from a cognitive radio channel is used to estimate the parameter of an HBMM in the maximum likelihood sense using a batch expectation-maximization algorithm [8], which is essentially the Baum algorithm [5]. The Baum algorithm involves both forward and backward recursions and iterates over a given sequence of observations. Given an HBMM parameter estimate, $\hat{\phi}$, forward recursions can be used to estimate the current state and predict a future state of the PU, given the current and past observation data. In Section 4.2, we develop a block-recursive online algorithm, which updates the HBMM parameter estimate after every m samples, where m denotes the block size. To perform state estimation and prediction in conjunction with the online parameter estimator, the same forward recursions developed in [40] can be applied, except that the HBMM parameter used in the recursions is dynamic, rather than static. This results in a fully online approach to temporal sensing, which does not require a training phase.

We next provide a brief outline of the state estimation and prediction scheme developed in [40]. To simplify notation, given a sequence $\{y_k\}$, we denote a subsequence $\{y_k, \ldots, y_n\}$, $k \leq n$, by y_k^n. When $k = 1$, we denote the subsequence y_1^n simply by y^n. Given an HBMM parameter ϕ, the conditional probability of the bivariate state Z_k given y^k, denoted by

$p_\phi(z_k \mid y^k)$, follows straightforwardly from the forward recursion for an HMM, (see, e.g., [40, Eq. (14)]). For an integer $\tau \geq 0$, the conditional probability of the bivariate state $Z_{k+\tau}$ given y^k is obtained from (see, e.g., [40, Eq. (22)]])

$$
\begin{aligned}
p_\phi(z_{k+\tau} \mid y^k) &= \sum_{z_k \in \mathbb{Z}} p_\phi(z_k \mid y^k) \, p_\phi(z_{k+\tau} \mid z_k) \\
&= \sum_{z_k \in \mathbb{Z}} \bar{\alpha}(z_k, y^k) \, [G^\tau]_{z_k, z_{k+\tau}} ,
\end{aligned}
\tag{4.4}
$$

where $\bar{\alpha}(z_k, y^k) = p_\phi(z_k \mid y^k)$ is computed using the scaled forward recursion for an HMM. Define a $dr \times dr$ block diagonal matrix $B(y_k)$, with its diagonal blocks given by $\{p(y_k \mid X_k = a)I, \ a \in \mathbb{X}\}$, for $k = 1, 2, \ldots$. The scaled forward recursion is given by (cf. [40, Eq. (14)])

$$
\bar{\alpha}_1 = \frac{\pi B(y_1)}{c_1}, \quad \bar{\alpha}_k = \frac{\bar{\alpha}_{k-1} G B(y_k)}{c_k}, \quad k = 2, 3, \ldots,
\tag{4.5}
$$

where $c_1 = \pi B(y_1)\mathbf{1}$, and $c_k = \bar{\alpha}_{k-1} G B(y_k)\mathbf{1}$.

A detection scheme for the state of the PU at time $k + \tau$ given the observation sequence y^k is specified as follows (cf. [40, Eq. (23)]):

$$
\hat{X}_{k+\tau|k} = \begin{cases} 1, & \text{if } \sum_{s_{k+\tau} \in \mathbb{S}} p_\phi(z_{k+\tau} = (1, s_{k+\tau}) \mid y^k) \geq \eta, \\ 2, & \text{otherwise}, \end{cases}
\tag{4.6}
$$

for $k = 1, 2, \ldots$, where η is a decision threshold, $0 < \eta < 1$. The detection scheme is a maximum a posteriori (MAP) detector when $\eta = 0.5$. When $\tau = 0$, $\hat{X}_{k+\tau|k} = \hat{X}_{k|k}$ is an estimate of the current state X_k. When $\tau = 1, 2, \ldots$, $\hat{X}_{k+\tau|k}$ is the τ-step predicted estimate of the state $X_{k+\tau}$. The current and predicted state estimates $\hat{X}_{k+\tau|k}$ can be directly applied to make dynamic spectrum access decisions.

The main thrust of this chapter lies in developing an online algorithm to update the

parameter estimate used in (4.6) at regular intervals. A fully online temporal spectrum sensing is obtained by executing (4.6) at each time step k with ϕ replaced by the most recent HBMM parameter estimate $\hat{\phi}_n$ computed by the online parameter estimator given by (4.8) in Section 4.2. The state estimation/prediction scheme (4.6) and the online parameter estimator (4.8) run in parallel. To quantitatively assess the performance of the online temporal spectrum sensing scheme, a receiver operating characteristic (ROC) curve can be obtained by determining the false alarm and missed detection probabilities for the scheme (4.6) corresponding to each value of η in the interval $(0, 1)$. Examples of such ROC curves are presented in Section 4.3.

4.2 Online Parameter Estimation Algorithm

In this section, we develop an efficient online parameter estimation algorithm for the HBMM. The algorithm extends an earlier online algorithm developed by Rydén for HMMs [47]. Other recursive parameter estimation schemes for HMMs have been proposed in the literature, notably the schemes proposed by Holst and Lindgren [19] and Krishnamurthy and Moore [25]. In contrast to these schemes, Rydén's algorithm is block-recursive and has lower computational complexity, as it does not involve scaling matrices. Moreover, numerical results presented in [47] show that estimates obtained using Rydén's scheme had much smaller variances than those obtained via the Holst-Lindgren procedure.

4.2.1 Rydén's block-recursive estimator for HMMs

Consider an HMM (Y, X), where X is a time-homogeneous Markov chain with state-space $\mathbb{X} = \{1, \ldots, d\}$ and Y is a sequence of conditionally independent random variables given X. In practice, the effect of the initial probability distribution π on the Markov chain quickly fades and accurate estimation of π is not necessary. Therefore, we parametrize the HMM by the row vector $\phi = [\mu_a, \sigma_a, g_{ab} : a, b \in \mathbb{X}]$. The total number of elements in ϕ is given by $L = 2d + d^2$, so we may write $\phi = [\phi_\ell : \ell = 1, \ldots, L]$. We also denote the space of HMM

parameters by $\Phi \subseteq \mathbb{R}^L$.

Rydén's algorithm operates on a block of observation data at a time. Let m denote the block size and let

$$\chi(y^m; \phi) = \frac{\partial \log p_\phi(y^m)}{\partial \phi} \tag{4.7}$$

be the score function associated with the joint density of Y^m under the parameter ϕ, denoted by $p_\phi(y^m)$. Here, χ is the $1 \times L$ gradient row vector of $\log p_\phi(y^m)$ with respect to ϕ. Rydén's recursive parameter estimator is based on a stochastic approximation algorithm of the following form:

$$\hat{\phi}_{n+1} = \Pi_{\mathcal{G}} \left[\hat{\phi}_n + \gamma_n \chi \left(y_{nm+1}^{(n+1)m}; \hat{\phi}_n \right) \right], \tag{4.8}$$

where $\Pi_{\mathcal{G}}$ denotes a projection operator, which is a mapping into a compact, convex set $\mathcal{G} \subseteq \Phi$. In the recursion (4.8), $\hat{\phi}_{n+1}$ is the $(n+1)$-st estimate of the HMM parameter, computed as a function of the observation samples $y_{nm+1}, \ldots, y_{(n+1)m}$ and the nth estimate $\hat{\phi}_n$. The sequence $\{\gamma_n\}$ is defined by $\gamma_n = \gamma_0 n^{-\varepsilon}$ for some $\gamma_0 > 0$ and $\varepsilon \in (\frac{1}{2}, 1]$. Under some mild assumptions, Rydén proved that the sequence $\{\hat{\phi}_n\}$ converges to a point lying in the set of Kuhn-Tucker points for minimizing the Kullback-Leibler divergence defined over $\mathcal{G}$. Assuming that the estimator (4.8) is consistent, it converges at a rate $n^{-\alpha/2}$ with $\alpha < 1$. Under some additional, relatively mild assumptions, Rydén showed that the averaged estimator

$$\bar{\phi}_n = \frac{1}{n} \sum_{k=1}^{n} \hat{\phi}_k \tag{4.9}$$

converges at rate $n^{-1/2}$ and is asymptotically normal. For convenience, we will simply refer to (4.8) as the online parameter estimator, with the understanding that the estimates $\hat{\phi}_n$ are averaged according to (4.9).

In practice, convergence of a parameter estimator could be measured in terms of a relative distance between consecutive parameter estimates, since the value of the true parameter is unknown. For example, one could use

$$\frac{||\hat{\phi}_{n-1} - \hat{\phi}_n||}{||\hat{\phi}_n||} < \omega_{th}, \tag{4.10}$$

where $|| \cdot ||$ denotes a norm and ω_{th} is an appropriate threshold. For comparison, we note that convergence of the batch Baum algorithm could be assessed through a relative distance between consecutive values of the likelihood function, which is readily available. Such likelihood function is not available for the online algorithm.

4.2.2 Online parameter estimator for HBMM

We next extend Rydén's algorithm by deriving a recursive procedure for computing the score function of an HBMM (Y, X, S), based on the approach of Willy et al. [58], which was originally developed for MMPPs. This results in an online parameter estimator for the HBMM. We remark that the theoretical convergence results established by Rydén for his recursive parameter estimation algorithm for the HMM carry over to the HBMM case, since an HBMM (Y, X, S), as defined in Section 4.1, is mathematically equivalent to an HMM (Y, U), where U is a univariate Markov chain with state space $\mathbb{U}$ isomorphic to $\mathbb{Z} = \mathbb{X} \times \mathbb{S}$. In spite of this mathematical equivalence, the specific details of the application of the HBMM yield the desired sojourn time phase-type distribution for this model, which is the primary advantage of the HBMM compared to the HMM.

The HBMM is parametrized by

$$\phi = [\mu_a, \ \sigma_a, \ g_{ab}(ij) : \ (a, i), (b, j) \in \mathbb{Z}].$$

We also denote the parameter by $\phi = [\phi_\ell : \ell = 1, \ldots, L]$, with $L = 2d + d^2r^2$. The score

function for the observed sequence y^m is the $1 \times L$ row vector given by

$$\chi(y^m; \phi) = \frac{1}{p_\phi(y^m)} \frac{\partial}{\partial \phi} p_\phi(y^m)$$

$$= \sum_{(b,j)\in\mathbb{Z}} \frac{1}{p_\phi(y^m)} \frac{\partial}{\partial \phi} p_\phi(y^m, z_m = (b,j)). \tag{4.11}$$

Let $H_m(y^m; \phi)$ denote a $dr \times L$ matrix whose (v, ℓ) element is given by

$$[H_m(y^m; \phi)]_{v\ell} = \frac{1}{p_\phi(y^m)} \frac{\partial}{\partial \phi_\ell} p_\phi(y^m, z_m = (b,j)), \tag{4.12}$$

where $(b, j) \in \mathbb{Z}$ such that $v = (b-1)r + j$ and $l \in \{1, \ldots, L\}$. Then the score function can be obtained from

$$\chi(y^m; \phi) = \mathbf{1}' H_m(y^m; \phi), \tag{4.13}$$

where $'$ denotes matrix transpose. Applying the conditional independence of the observation sequence Y given the underlying Markov chain Z yields $[H_m(y^m; \phi)]_{v\ell}$ as

$$\frac{1}{p_\phi(y^m)} \frac{\partial}{\partial \phi_\ell} \sum_{(a,i)\in\mathbb{Z}} p_\phi(y^{m-1}, z_{m-1} = (a,i)) f_{ij}^{ab}(y_m; \theta_b)$$

$$= \frac{1}{p_\phi(y_m \mid y^{m-1})} \sum_{(a,i)\in\mathbb{Z}} \frac{1}{p_\phi(y^{m-1})} \cdot \frac{\partial}{\partial \phi_\ell} \left[p_\phi(y^{m-1}, z_{m-1} = (a,i)) f_{ij}^{ab}(y_m; \theta_b) \right], \tag{4.14}$$

where $f_{ij}^{ab}(y_m; \theta_b) \triangleq g_{ab}(ij) f(y_m; \theta_b)$. Comparing (4.12) and (4.14), a recursive procedure for computing $H_m(y^m; \phi)$ can be obtained as follows:

$$\left[H_k(y^k; \phi) \right]_{v\ell} = \frac{1}{c_k} \sum_{(a,i)\in\mathbb{Z}} \left\{ \left[H_{k-1}(y^{k-1}; \phi) \right]_{u\ell} \cdot \right.$$

$$\left. f_{ij}^{ab}(y_k; \theta_b) + \xi_{k-1}(a,i) \frac{\partial}{\partial \phi_\ell} f_{ij}^{ab}(y_k; \theta_b) \right\}, \tag{4.15}$$

43

for $k = 1, 2, ..., m$, where $u = (a-1)r + i$ and

$$\xi_k(b, j) \triangleq p_\phi(z_k = (b, j) \mid y^k) = \frac{1}{c_k} \sum_{(a,i) \in \mathbb{Z}} \xi_{k-1}(a, i) f_{ij}^{ab}(y_k; \theta_b), \tag{4.16}$$

$$c_k \triangleq p_\phi(y_k \mid y^{k-1}) = \sum_{(a,i) \in \mathbb{Z}} \sum_{(b,j) \in \mathbb{Z}} \xi_{k-1}(a, i) f_{ij}^{ab}(y_k; \theta_b). \tag{4.17}$$

Let ξ_k be a $1 \times dr$ row vector given by

$$\xi_k = [\xi_k(a, i) : (a, i) \in \mathbb{Z}] \tag{4.18}$$

and define a $dr \times dr$ matrix

$$F(y_k) = [f_{ij}^{ab}(y_k; \theta_b) : (a, i), (b, j) \in \mathbb{Z}]. \tag{4.19}$$

Then (4.16) and (4.17) can be expressed more compactly as

$$\xi_k = \frac{1}{c_k} \xi_{k-1} F(y_k), \tag{4.20}$$

and

$$c_k = \xi_{k-1} F(y_k) \mathbf{1}, \tag{4.21}$$

respectively. Equation (4.15) can then be expressed in matrix form as follows, starting from the initial condition $H_0(y^0; \phi) = \mathbf{0}$, where $\mathbf{0}$ denotes a $dr \times L$ zero matrix:

$$H_k(y^k; \phi) = \frac{1}{c_k} \left\{ F(y_k)' H_{k-1}(y^{k-1}; \phi) + (I \otimes \xi_{k-1}) \frac{\partial}{\partial \phi} [\text{vec } F(y_k)]' \right\}, \tag{4.22}$$

where I denotes an identity matrix, of order dr in this case, $\otimes$ denotes the Kronecker product, and vec $F(y_k)$ denotes the $d^2 r^2 \times 1$ column vector obtained by stacking the columns

44

of the matrix $F(y_k)$ one on top of the other. The form of (4.22) is particularly convenient for implementing the online parameter estimator in a vector-based programming language such as MATLAB. The $d^2 r^2 \times L$ matrix $\partial [\text{vec } F(y_k)]'/\partial \phi$ is the Jacobian of the vector-valued function $[\text{vec } F(y_k)]'$ with respect to the HBMM parameter ϕ. The elements of the $d^2 r^2 \times L$ Jacobian matrix $\partial [\text{vec } F(y_k)]'/\partial \phi$ are partial derivatives of $f_{ij}^{ab}(y_k; \theta_b)$, given as follows:

$$\frac{\partial f_{ij}^{ab}(y_k; \theta_b)}{\partial [g_{ce}(\iota l)]} = f(y_k; \theta_b) \, \mathbf{1}_{\{(c,\iota)=(a,i),(e,l)=(b,j)\}}, \tag{4.23}$$

$$\frac{\partial f_{ij}^{ab}(y_k; \theta_b)}{\partial (\sigma_c)} = f_{ij}^{ab}(y_k; \theta_b) \frac{(y_k - \mu_b)^2 - \sigma_b^2}{\sigma_b^3} \, \mathbf{1}_{\{c=b\}}, \tag{4.24}$$

$$\frac{\partial f_{ij}^{ab}(y_k; \theta_b)}{\partial (\mu_c)} = f_{ij}^{ab}(y_k; \theta_b) \frac{y_k - \mu_b}{\sigma_b^2} \, \mathbf{1}_{\{c=b\}}, \tag{4.25}$$

for $(c, \iota), (e, l) \in \mathbb{Z}$, where $\mathbf{1}_A$ denotes an indicator function on the set A.

The computational complexity of the online estimator at each step is dominated by the computation of the matrix $H_m(y^m; \phi)$ in (4.22), which requires $O((d^3 r^3)L) = O(d^5 r^5)$ arithmetic operations for the HBMM, assuming a straightforward sequential implementation. For the spectrum sensing application, $d = 2$, so the complexity of the estimator grows as $O(r^5)$. In practice, a larger value of r can yield more accurate parameter estimates, but then more observation data would be required for the estimator to converge. In our numerical experiments, we have used values of r ranging from 1 to 5. We remark that each iteration of the Baum algorithm proposed in [40] has computational complexity $O(r^2 T)$, where T is the length of the observation sequence used to compute the estimate and is typically quite large (e.g., $T = 2000$). Furthermore, the Baum algorithm may require many iterations to converge.

4.3 Numerical Results

In this section, we presents the results of a numerical study to assess the accuracy of the proposed algorithm in estimating the parameter of an HBMM and in estimating the state of the PU for online spectrum sensing.

4.3.1 Implementation

The online HBMM parameter estimator was implemented in MATLAB. The block size is chosen to be $m = 20$ and the averaging procedure (4.9) is started after the basic recursion (4.8) has been executed for $1,000$ steps. For the projection step in (4.8), we define the parameter space $\mathcal{G}$ as follows:

$$\mathcal{G} = \{\phi : \mu_a \in (\underline{\mu}, \bar{\mu}), \sigma_a \in (0, \bar{\sigma}), g_{ab}(ij) \in (\underline{g}, \bar{g}),$$

$$\sum_{(b,j) \in \mathbb{Z}} g_{ab}(ij) = 1; (a, i), (b, j) \in \mathbb{Z}\}, \tag{4.26}$$

where $\underline{\mu} = -10^6$, $\bar{\mu} = 10^6$, $\bar{\sigma} = 100$, $\underline{g} = 10^{-6}$, and $\bar{g} = 1 - 10^{-6}$. The projection operator $\Pi_{\mathcal{G}}$ in (4.8) can be implemented in various ways. We have obtained good results using the following approach. Let $\tilde{\phi}$ denote the bracketed expression in (4.8). Recall that the parameter ϕ is the triplet $[\mu, \sigma, G]$. The components of $\hat{\phi}_{n+1}$ are obtained from the corresponding components of $\tilde{\phi}$ using

$$\hat{\mu}_a^{(n+1)} = \begin{cases} \tilde{\mu}_a, & \tilde{\mu}_a \in (\underline{\mu}, \bar{\mu}), \\ \hat{\mu}^{(n)}, & \text{otherwise}, \end{cases}$$

$$\hat{\sigma}_a^{(n+1)} = \begin{cases} \tilde{\sigma}_a, & \tilde{\sigma}_a \in (\underline{\sigma}, \bar{\sigma}), \\ \hat{\sigma}^{(n)}, & \text{otherwise}, \end{cases}$$

for $a \in \mathbb{X}$ and

$$\hat{g}_{ab}^{(n+1)}(ij) = \frac{\hat{g}_{ab}(ij)}{\sum_{(b,j) \in \mathbb{Z}} \hat{g}_{ab}(ij)}, \tag{4.27}$$

where

$$\hat{g}_{ab}(ij) = \begin{cases} \hat{g}_{ab}^{(n)}(ij)(1 + \tilde{g}_{ab}(ij) - \hat{g}_{ab}^{(n)}(ij)), & \tilde{g}_{ab}(ij) \in (\underline{g}, \bar{g}), \\ \hat{g}_{ab}^{(n)}(ij), & \text{otherwise,} \end{cases} \tag{4.28}$$

for $(a, i), (b, j) \in \mathbb{Z}$. The heuristic expression for $\hat{g}_{ab}^{(n+1)}(ij)$ given by (4.27) and (4.28) provides a numerically stable estimator for the transition matrix and allows a more aggressive weighting sequence $\{\gamma_n\}$ to be chosen in the recursive procedure (4.8) to achieve faster convergence. In our implementation, we set $\gamma_n = \gamma_0 n^{-\varepsilon}$, where $\gamma_0 = 0.3$ and $\varepsilon = 0.35$. Note that in our approach, the projection operator $\Pi_{\mathcal{G}}$ appearing in (4.8) depends on $\hat{\phi}_n$. In our numerical studies, we have found that computing estimates of all components of the transition matrix G via (4.8) and then normalizing, as in (4.27), results in significantly better performance than computing estimates of only the independent components of G. This provides a practical justification for retaining the entire transition matrix as part of the HBMM parameter.

4.3.2   Simulation setup

For our spectrum sensing simulations, the true parameter ϕ^0 of the HBMM was the one used in [40]. That parameter was estimated from real spectrum measurements of a paging channel collected in [49] using the Baum algorithm. The 20×20 transition matrix of that parameter is given in Appendix A.1. The parameter components for the conditionally normal distributions are given in Table 4.1. This HBMM parameter was used to generate the ground truth observation sequence in most of our numerical experiments.

We varied the order r of the HBMM estimate, as well as the length T of the observation

Table 4.1: Estimates of HBMM parameter components for the observable process.

	true	Baum	$r = 1$	$r = 2$	$r = 5$
$\hat{\mu}_1$	-112.40	-112.38	-112.49	-112.50	-112.43
$\hat{\sigma}_1$	3.77	3.79	3.75	3.73	3.74
$\hat{\mu}_2$	-45.61	-45.67	-45.62	-45.57	-45.62
$\hat{\sigma}_2$	1.77	1.77	1.78	1.76	1.77

sequence generated by the true parameter. We set the initial parameter ϕ^s using a randomly generated transition matrix G^s. In our simulation experiments, the initial values of the HBMM parameter components associated with the conditionally Gaussian observable sequence are given by $(\mu_1^s, \sigma_1^s) = (-120, 1)$ and $(\mu_2^s, \sigma_2^s) = (-80, 2.24)$. The choice of the order r involves a tradeoff among model accuracy, computational efficiency, and the number of observation samples required to obtain a "good" estimate. Choosing a larger value of r generally requires more observation samples and computation, but can potentially result in better estimates. Estimating the transition matrix G is a much more difficult task than estimating the conditionally normal parameter components. Unless the initial transition matrix G^s is somewhat close to the true transition matrix G, the estimate $\hat{G}$ typically appears to be a rather poor representation of G. Nevertheless, the sojourn time distributions derived from $\hat{G}$ tend to closely approximate the true sojourn time distributions, given a sufficient number of observation samples. For the spectrum sensing application, accuracy of the sojourn time distribution estimates, as obtained from the parameter estimate using (4.3), is of primary concern, as opposed to convergence of the parameter estimates themselves [40]. Therefore, our results focus on the quality of the estimated sojourn time distributions rather than on convergence of the estimates of the transition matrix.

4.3.3 Results

We have tested the recursive parameter estimator developed in this chapter, and compared its performance with the Baum algorithm proposed in [38, 40]. We have run the Baum

algorithm on $T = 2000$ observations using a predetermined fixed number of iterations. This number was determined by the ratio of the total number of observations available to the recursive algorithm, and $T = 2000$. This approach allows us to compare the two estimators using effectively the same number of observations. For $r = 1, 2$, and 5, the number of Baum iterations was set to $5, 10$ and 25, respectively.

The estimated values of the components of the parameter which correspond to the conditional Gaussian distributions, as obtained by the Baum algorithm, are shown in Table 4.1 in the column labelled 'Baum'. We ran the online algorithm for the same values of $r = 1, 2, 5$ with observation sequence lengths of 10000, 20000, and 50000, respectively. The estimates of (μ_a, σ_a) in this case are given in the columns marked $r = 1$, $r = 2$, and $r = 5$, respectively, in Table 4.1. In all cases, the estimates were very close to the true parameter values. These results underscore the relative ease with which the conditionally Gaussian parameter components can be estimated.

Estimation of the transition matrix of the true model of order $r = 10$, by either the recursive algorithm or the Baum algorithm, has proven to be a much harder task. Our numerical work suggests that for smaller order r of the true parameter, e.g., $r = 2, 3$, both algorithms often converge to an estimate close to ϕ^0, but this is not the case for higher orders. For the spectrum sensing application, however, the accuracy of the estimates is measured by their ability to represent the sojourn times in the active and idle states. Both the recursive and the Baum algorithms provided accurate estimates in this respect for higher model orders of the true parameter, in particular, for $r = 10$.

The sojourn time distributions associated with the estimates of G obtained by applying the online and Baum algorithms for $r = 1, 2, 5$ are shown in Figs. 4.1, 4.2, and 4.3, respectively. For a given parameter estimate, the associated sojourn time distribution is given by (4.3). When $r = 1$, i.e., when the HBMM is an HMM, the estimated idle $(X_k = 1)$ and active $(X_k = 2)$ state sojourn time distributions appear to be very different from the true ones. The online and Baum algorithms seem to perform similarly in this case. For $r = 2$, the estimated idle state sojourn time distributions obtained using the two algorithms lines
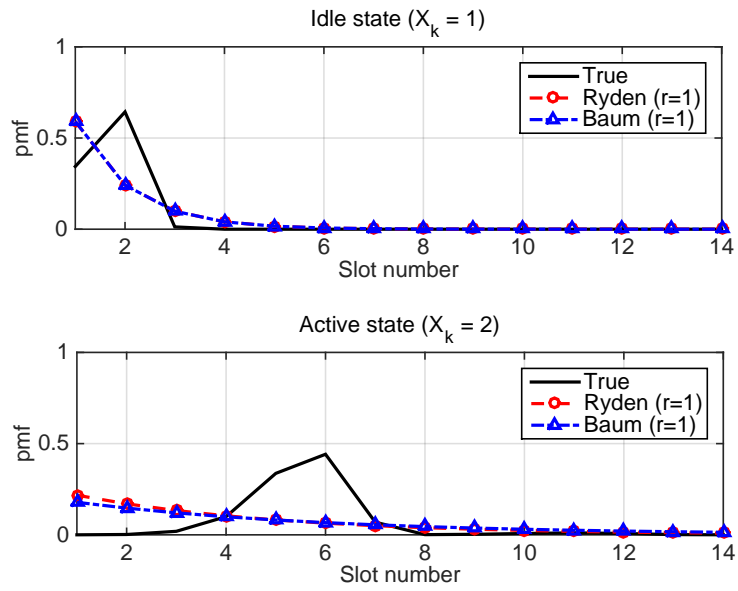
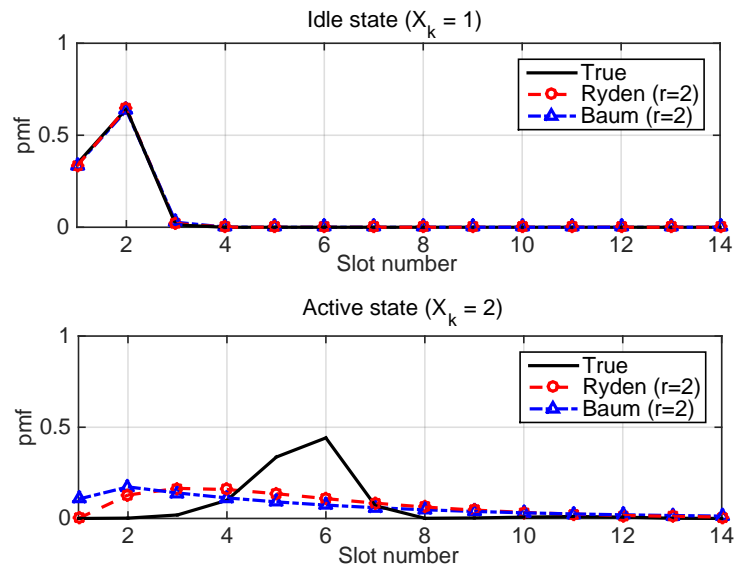Figure 4.1: Estimated sojourn time distributions, $r = 1$ (HMM).

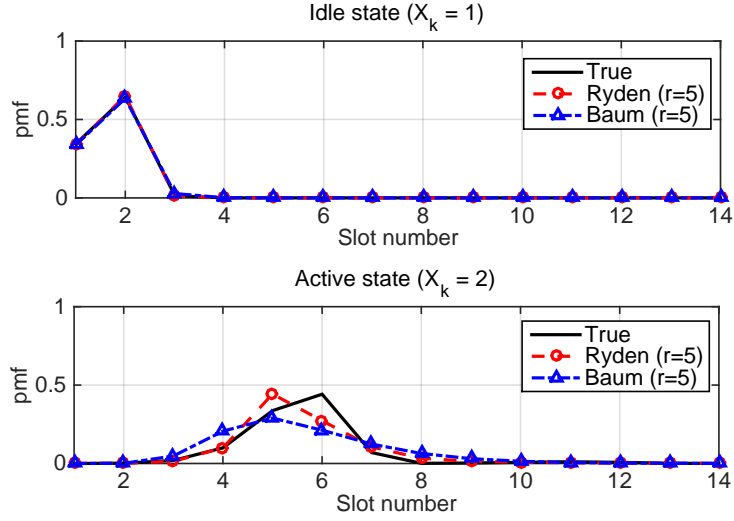Figure 4.2: Estimated sojourn time distributions, $r = 2$.

Figure 4.3: Estimated sojourn time distributions, $r = 5$.

up very closely with the true distribution. For the active state distribution, the estimates obtained using the online and Baum algorithms are still far from the true distribution, but some improvement can be observed relative to the case $r = 1$. Significant improvement in the active state sojourn time distribution estimate can be seen when $r = 5$. In this case, the online estimate is superior to the Baum estimate. We note that by increasing the number of iterations, the Baum algorithm will eventually obtain an estimated sojourn time distribution which closely matches that obtained by the online algorithm (cf. Fig. 8 in [40]). To converge in this sense, the Baum algorithm required 15 iterations when $r = 2$ and 50 iterations when $r = 5$.

The recursive algorithm can also be applied repeatedly to a fixed observation sequence in an offline setup similar to that of the Baum algorithm. We applied this alternative offline algorithm, which we refer to as 'online-rep,' to a sequence of $T = 2000$ observation samples and 10 and 25 iterations for model orders of $r = 2$ and 5, respectively. This is equivalent to applying the online algorithm to observation sequences of lengths $20,000$ and $50,000$, obtained by concatenating the same sequence of 2000 observation samples 10 and 25 times, respectively. We found that the accuracy of the sojourn time distribution estimates obtained
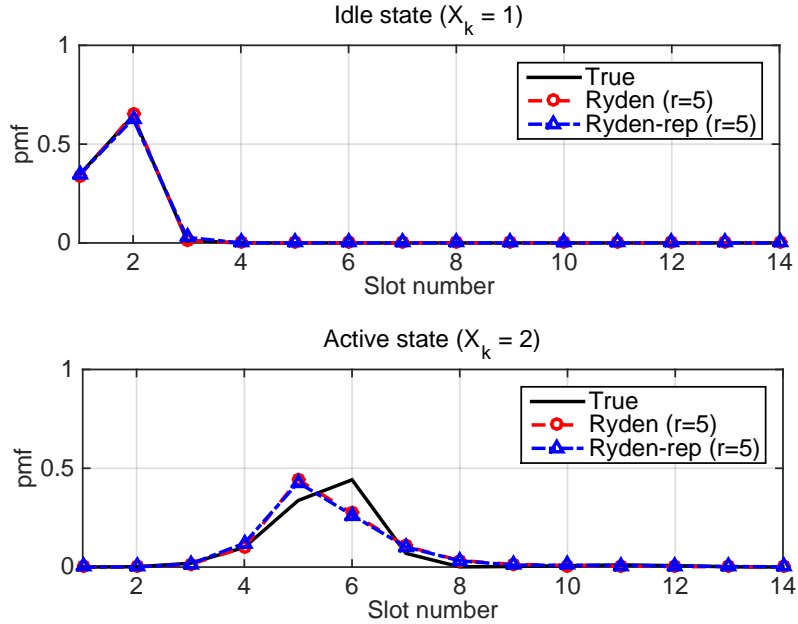
Figure 4.4: Estimated sojourn time distributions, $r = 5$.

using 'online-rep' was very similar to that obtained by applying the online algorithm to sequences of length $20,000$ and $50,000$ generated, respectively, using the true parameter. Fig. 4.4 compares the estimated sojourn time distributions obtained using 'online-rep' vs. those obtained using the online algorithm (labelled 'online' as before). The two sojourn time distributions are very close to each other and both are more accurate than the estimated sojourn time distributions obtained using an equivalent application of the Baum algorithm (see Fig. 4.3). Relative to the 'online-rep' algorithm, the Baum algorithm required 50% more iterations when $r = 2$ and 200% more iterations when $r = 5$ to obtain the converged sojourn time distribution estimates.

An important advantage of the online parameter estimator relative to the Baum algorithm is that it can adapt to changes in the true parameter. To demonstrate this feature, we created an observation sequence consisting of $80,000$ samples generated using of the true parameter of order $r = 10$ as above, followed by $80,000$ samples generated using a different HBMM parameter of order $r = 3$ whose transition matrix is given in Appendix
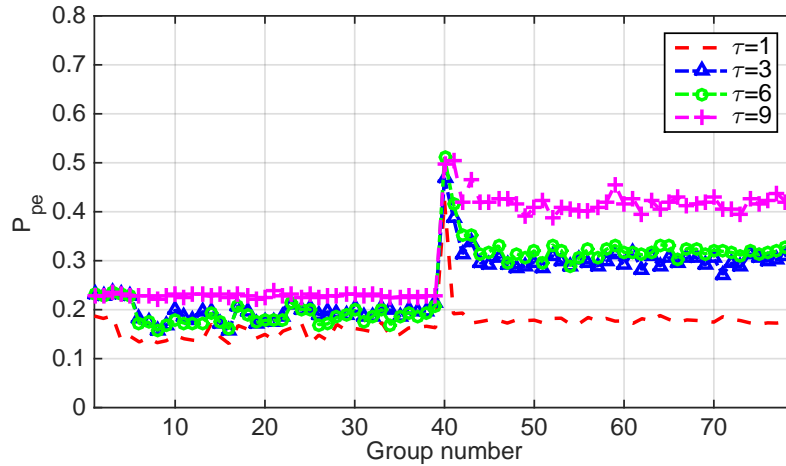
52

Figure 4.5: τ-step error probability for the state prediction scheme ($r = 5, \eta = 0.5$) vs. observation group number.

A.2. The sojourn time distributions in the idle and active states of the second HBMM were identical. Consequently, the PU is in the idle and active states with equal probability, which makes state estimation and prediction more difficult in the case of the second HBMM model, relative to the first.

The recursive state prediction scheme (4.6) together with the online parameter estimator (4.8), using an HBMM of order $r = 5$ and with $\eta = 0.5$, were applied to the concatenated observation sequence of $160,000$ samples, The observation sequence was divided into 80 groups of 2000 samples each. Fig. 4.5 shows the real-time τ-step state prediction performance ($\tau = 1, 3, 6, 9$) of the spectrum sensing scheme. The horizontal axis indicates the group number, while the vertical axis represents the error probability of the prediction scheme (4.6), P_{pe}, computed by averaging over each group of 2000 observation samples. The online parameter estimator is initialized with a randomly chosen initial parameter. At group number 40, the model changes to the second HBMM parameter and a spike in P_{pe}, as expected, can be observed for all values of τ. For $\tau = 1$, the error probability drops quickly at group 41 and reaches a steady-state level of about 0.18 after an additional 2–3 groups of observation samples. For the other values of τ, the error performance takes 1–2 additional
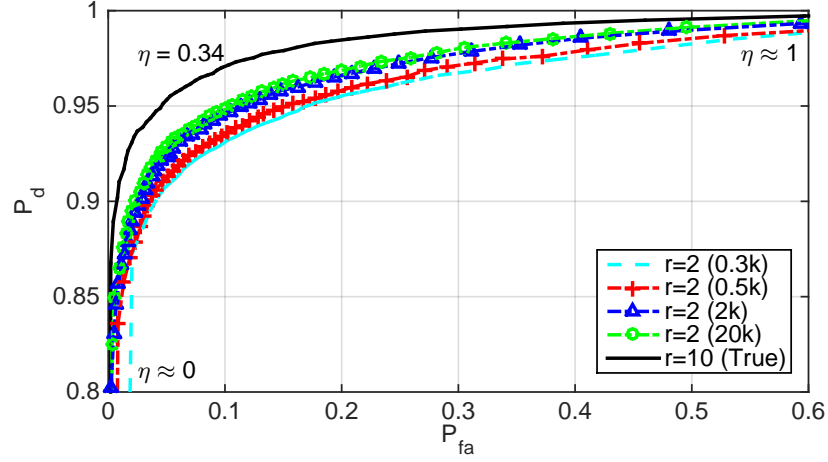
Figure 4.6: ROC plot, $r = 2$.

groups of observation samples to attain steady-state. To summarize, the error performance of the state prediction scheme required fewer than 6000 observation samples to converge to steady-state. On the other hand, as noted earlier, for the same order $r = 5$, about $50,000$ observation samples were required for the sojourn time distribution estimates to converge. Thus, the error performance of the state prediction scheme converges much faster than the sojourn time distribution estimates.

To gain further insight into the performance of the proposed online spectrum sensing scheme, we consider the ROC performance of the state estimator given by (4.6) when $\tau = 0$. We use an HBMM parameter with the same transition matrix G for $r = 10$ as before, but the parameters of the observable process are modified to reflect a more prominent shadowing effect in the wireless channel as in [40, Eq. (26)], as follows:

$$(\mu_1, \sigma_1) = (-112.40, 3.77), \quad (\mu_2, \sigma_2) = (-95.40, 8.19). \tag{4.29}$$

To obtain a ROC curve, we simulate a set of sample paths of an HBMM characterized by the true parameter ϕ^0. For each sample path, the online parameter estimator (4.8) and the state detection scheme in (4.6), with a fixed detection threshold η, are applied. The false alarm and missed detection probabilities corresponding to the fixed value of η are computed
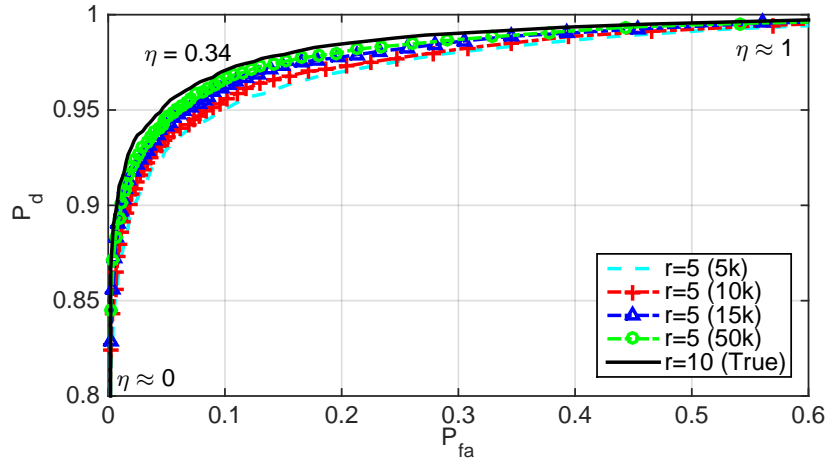
54

Figure 4.7: ROC plot, $r = 5$.

by averaging over the set of samples paths. This procedure is repeated for values of η in the interval $(0, 1)$ to obtain the ROC curve.

Figure 4.6 shows a family of ROC curves for parameter estimates of order $r = 2$ obtained by applying the online procedure to observation sequences of length 300, 500, 2000, and 20,000 (labelled 0.3k, 0.5k, 2k, and 20k, respectively), which were generated using the modified HBMM parameter of order $r = 10$. For a given parameter estimate, a ROC curve was obtained by applying the state estimator in (4.6) with each new observation group of length 20,000. Observe that the parameter estimates labelled 2k and 20k have similar ROC performance. We also see that the ROC curves labelled 0.3k and 0.5k are close to each other, while not being significantly far from the 2k curve. These results suggest that it is not necessary for the sojourn time distribution estimates to converge in order to achieve good ROC performance; i.e., given a relatively small number of observation samples, the online estimator yields estimates with acceptable ROC performance. We remark that the ROC plots in Figs. 4.6 and 4.7 are relatively insensitive to the choice of initial parameter for the estimators.

Figure 4.7 shows a family of ROC curves obtained using parameter estimates of order $r = 5$. In this case, five parameter estimates were obtained using observation sequences

of length 5000, $10,000$, $15,000$, and $50,000$ (labelled 5k, 10k, 15k, and 50k, respectively). All of these curves show superior performance relative to the order $r = 2$ estimates from Fig. 4.6. On the other hand, more observation samples are generally needed to obtain good parameter estimates for higher values of the model order r. There is a clear gap between the 5k and 50k curves, but the difference between the curves is relatively small. This again suggests that even with a relatively small number of observation samples, the online parameter estimator provides parameter estimates, which in combination with the recursive state estimation scheme, result in good ROC performance.

Chapter 5: Collaborative Spectrum Sensing

In this chapter, we focus on the collaborative spectrum sensing in cognitive radio network to make more reliable spectrum sensing. In radio environments with severe shadowing and fading effects, spectrum sensing by a single SU can lead to hidden terminal effects and other errors which can result in harmful interference to the PUs.

Collaboration among SUs can address this hidden terminal problem by exploiting the spatial diversity. In this chapter, we first briefly review the conventional hard fusion schemes and linear soft fusion scheme. Then we incorporate the HBMM model based spectrum sensing into these fusion schemes. Finally, we propose a quantized HBMM soft fusion scheme to improve the spectrum sensing performance while minimizing the network overhead. The work in this chapter appears in [52] and [55].

5.1 System Model

We consider a system consisting of one PU transmitting on a given narrowband channel and Q SUs performing collaborative spectrum sensing on the channel. The PU alternates between active state in which a signal is transmitted and an idle state in which no signal is transmitted. Each SU performs spectrum sensing and computes the received power from the PU. The state of the PU is represented by a discrete-time process $X = \{X_k; k = 1, 2, \ldots\}$ such that at time k the state of the PU is given by the random variable

$$X_k = \begin{cases} 1, & \text{idle state,} \\ 2, & \text{active state.} \end{cases} \tag{5.1}$$
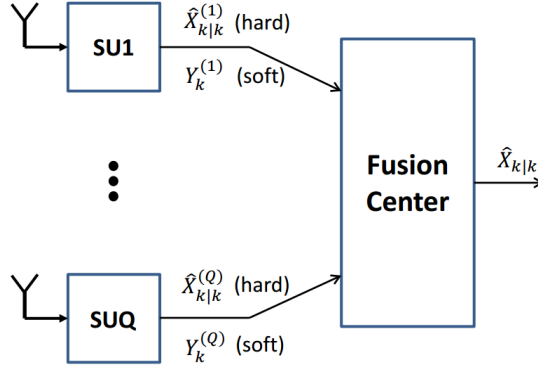
Figure 5.1: A generic collaborative sensing scheme.

The state space of the PU is given by $\mathbb{X} = \{1, 2\}$. Assuming a standard path loss plus log-normal shadowing model, the received signal power $Y_k^{(q)}$, in units of dBm, can be expressed as follows (cf. [54]):

$$
Y_k^{(q)} = \begin{cases} \mu_1^{(q)} + \epsilon_{1,\text{dB}}^{(q)}, & X_k = 1, \\ \mu_2^{(q)} + \epsilon_{2,\text{dB}}^{(q)}, & X_k = 2, \end{cases}
\tag{5.2}
$$

where $\mu_a^{(q)}$ represents the mean received signal power of the qth SU when the PU is in state $a \in \{1, 2\}$ and $\epsilon_{a,\text{dB}}^{(q)}$ is a zero-mean Gaussian random variable with standard deviation $\sigma_a^{(q)}$, which represents lognormal normal shadowing. The received signal powers may undergo further processing, such as local averaging [33] and quantization, but we shall still use the notation $Y_k^{(q)}$ to denote the processed observations.

A block diagram of a generic collaborative sensing scheme is shown in Fig. 5.1. In soft fusion, at each time k, the SUs transmit their received signals $Y_k^{(1)}, \ldots, Y_k^{(q)}$, to the fusion center, where they are used to estimate the state of the PU at time $k + \tau$ for some nonnegative integer τ. The state estimator is denoted by $\hat{X}_{k+\tau|k}$ and takes values in $\mathbb{X}$. For conventional fusion schemes that do not have predictive capability, $\tau = 0$. In a *linear*

soft fusion scheme, a weighted sum, $V_k = \sum_{q=1}^{Q} w_q Y_k^{(q)}$, of the observations at time k is computed and compared to a threshold ψ as follows [32, 43, 44]:

$$\hat{X}_{k|k} = \begin{cases} 1, & V_k < \psi, \\ 2, & V_k \geq \psi, \end{cases} \tag{5.3}$$

where $w_1, \ldots w_Q$ are the weights. Typically, the threshold and weights for soft fusion are computed offline [32, 44].

In [44], an approach to computing the weights for linear soft fusion was proposed, based on maximizing a so-called modified deflection coefficient (MDC). Numerical results showed that this approach achieved near-optimal detection performance for linear soft fusion. Let $\boldsymbol{w} = (w_1, \ldots, w_Q)$ denote the vector of weights. Define $\boldsymbol{\mu}_a = (\mu_a^{(q)} : q = 1, \ldots, Q)$ for $a \in \mathbb{X}$. The channels observed by the SUs are assumed to be conditionally independent given the PU state. Under this assumption, the conditional covariance matrix is given by $\Sigma_a = \text{diag}([\sigma_a^{(q)}]^2 : q = 1, \ldots, Q)$. Then the optimal MDC weight vector derived in [44] is given by

$$\boldsymbol{w} = \frac{\Sigma_2^{-1} \boldsymbol{\mu}'}{\|\Sigma_2^{-1} \boldsymbol{\mu}'\|_2}, \tag{5.4}$$

where $\boldsymbol{\mu} = \boldsymbol{\mu}_2 - \boldsymbol{\mu}_1$. In Section 5.3, we compare the performance of the proposed HBMM soft fusion scheme against linear soft fusion based on (5.4). The HBMM soft fusion approach is not restricted to linear estimation, and the state of the PU is estimated from current and previous observations from all SUs.

In a hard fusion scheme, at each time k, each SUq makes an independent decision on the PU state based on the observations $Y_1^{(q)}, \ldots, Y_k^{(q)}$. The 1-bit SU hard decisions are transmitted to the fusion center, which computes a final decision, $\hat{X}_{k|k}$, according to a hard fusion rule. For example, the "OR" rule decides that the PU is active, i.e., state 2, if at

least one of the SU hard decisions has the value 2. The "majority voting" rule decides that the PU is active if more than half of the Q SU hard decisions have value 2. The OR-rule and majority voting rule are special cases of the q-out-of-Q rule, where $q \geq 0$ is an integer constant. Here, the PU state is determined to be active if q or more of the hard decisions are 'active'; otherwise, the PU state is determined to be idle. The OR and majority voting rules are equivalent to the q-out-of-Q rule when $q = 1$ and $q = \lfloor Q/2 \rfloor$, respectively. The q-out-of-Q fusion rule is in turn a special case of linear hard fusion (cf. [43]). Under linear combining, the decision variable is computed as $V_k = \sum_{q=1}^{Q} w_q X_k^{(q)}$, where the w_q are predetermined weights. The decision variable V_k is then compared to a threshold ψ to obtain the final decision $\hat{X}_{k|k}$ as in (5.3). The q-out-of-Q fusion rule is a special case of hard linear fusion.

In conventional hard fusion schemes, each SU employs an energy detector to obtain a hard decision at each time k, i.e., SUq estimates the PU state as follows:

$$
\hat{X}_{k|k}^{(q)} = \begin{cases} 1, & Y_k^{(q)} < \psi_q, \\ 2, & Y_k^{(q)} \geq \psi_q, \end{cases} \tag{5.5}
$$

where ψ_q denotes a threshold, which is usually computed offline. Typically, a majority voting rule is applied at the fusion center. In the HBMM hard fusion scheme, the state estimate $\hat{X}_{k|k}^{(q)}$ for each SUq is a function of the current and previous observations, not just the current sample $Y_k^{(q)}$. In addition, the HBMM hard fusion scheme employs a linear fusion rule based on the MDC weight vector given by (5.4).

5.2 Collaborative Sensing Schemes

5.2.1 HBMM soft fusion

Referring to Fig. 5.2, at each time k, the observation sample $Y_k^{(q)}$ from each SUq is transmitted directly to the fusion center, which forms the *vector* observation sample $\boldsymbol{Y}_k =$
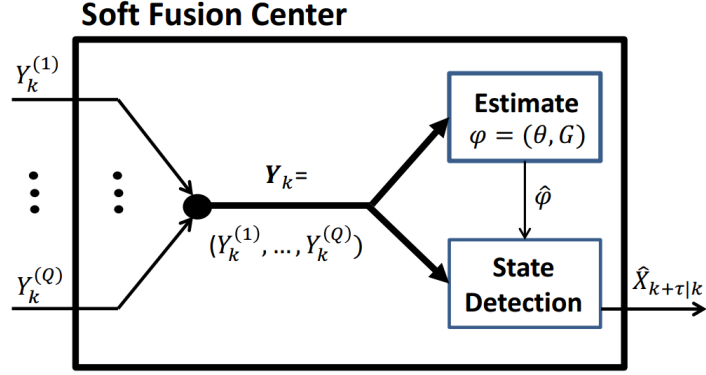
Figure 5.2: HBMM soft fusion.

$(Y_k^{(1)}, \ldots, Y_k^{(Q)})$. The proposed soft fusion scheme is based on hidden bivariate Markov chain modeling of the *vector* observation sequence $\boldsymbol{Y} = \{\boldsymbol{Y}_k; k = 1, 2, \ldots\}$ generated by the Q SUs. Here, the conditional output density parameter is given by $\boldsymbol{\theta} = (\boldsymbol{\theta}_a : a \in \mathbb{X})$, where $\boldsymbol{\theta}_a = (\theta_a^{(1)}, \ldots, \theta_a^{(Q)})$, and $\theta_a^{(q)}$ is the conditional output density parameter of each SUq when the PU is in state a. With this definition of $\boldsymbol{\theta}$, the parameter of the HBMM is given formally by $\phi = (\boldsymbol{\theta}, G)$, which we also denote by $\phi = [\phi_\ell : \ell = 1, \ldots, L]$, where $L = 2dQ + d^2 r^2$.

Recursions for online parameter and state estimation of the HBMM in the setup of Fig. 5.2 with vector observation input can be obtained from temporal spectrum sensing, by replacing the scalar sequence y^k by the vector sequence $\boldsymbol{y}^k$ and θ by $\boldsymbol{\theta}$. To compute $f(\boldsymbol{y}_k; \boldsymbol{\theta}_b)$, we assume that the Q cognitive radio channels are conditionally independent given the state of the PU, in which case, $f(\boldsymbol{y}_k; \boldsymbol{\theta}_b) = f(y_k^{(1)}; \theta_b^{(1)}) \cdot f(y_k^{(2)}; \theta_b^{(2)}) \cdots f(y_k^{(Q)}; \theta_b^{(Q)})$. The elements

of the $d^2r^2 \times L$ Jacobian matrix $\partial[\text{vec } F(\boldsymbol{y}_k)]'/\partial\phi$ are given as follows:

$$\frac{\partial}{\partial[g_{ce}(\iota l)]} f_{ij}^{ab}(\boldsymbol{y}_k; \boldsymbol{\theta}_b) = f(\boldsymbol{y}_k; \boldsymbol{\theta}_b) \, \mathbf{1}_{\{(c,\iota)=(a,i),(e,l)=(b,j)\}},$$

$$\frac{\partial}{\partial(\mu_c^{(q)})} f_{ij}^{ab}(\boldsymbol{y}_k; \boldsymbol{\theta}_b) = f_{ij}^{ab}(\boldsymbol{y}_k; \boldsymbol{\theta}_b) \frac{y_k^{(q)} - \mu_b^{(q)}}{(\sigma_b^{(q)})^2} \, \mathbf{1}_{\{c=b\}},$$

$$\frac{\partial}{\partial(\sigma_c^{(q)})} f_{ij}^{ab}(\boldsymbol{y}_k; \boldsymbol{\theta}_b) = f_{ij}^{ab}(\boldsymbol{y}_k; \boldsymbol{\theta}_b) \cdot \frac{(y_k^{(q)} - \mu_b^{(q)})^2 - (\sigma_b^{(q)})^2}{(\sigma_b^{(q)})^3} \, \mathbf{1}_{\{c=b\}}, \tag{5.6}$$

for $(c, \iota), (e, l) \in \mathbb{Z}$. When the state recursion (4.5) is generalized for vector observation input, the matrix $B(y_k)$ is replaced by the $dr \times dr$ block diagonal matrix $B(\boldsymbol{y}_k) = B(y_k^{(1)}) \cdot B(y_k^{(2)}) \cdots B(y_k^{(Q)})$, where $B(y_k^{(q)})$ is a $dr \times dr$ block diagonal matrix with diagonal blocks given by $\{p(y_k^{(q)} \mid X_k = a)I, \; a \in \mathbb{X}\}$, for $k = 1, 2, \ldots$. The product form of $B(\boldsymbol{y}_k)$ follows from assuming conditional independence of the cognitive radio channels given the state of the PU.

The complexity of the HBMM soft fusion scheme in each time slot is dominated by the computation of $H_m(\boldsymbol{y}^m; \phi)$, which requires $O(d^3 r^3 \cdot (2dQ + d^2 r^2)) = O(d^4 r^3 Q + d^5 r^5) = O(r^3 Q + r^5)$ when $d = 2$. Since Q is a small constant in practice, the overall complexity of the proposed soft fusion scheme is essentially the same as that of the hard fusion scheme. If the linear combination weights and decision threshold are precomputed, the complexity of soft linear fusion becomes only $O(Q)$. However, if these parameters are estimated online using HBMM parameter estimation, as proposed in [52], the complexity of the online soft linear fusion scheme per time slot becomes $O(r^5)$.

5.2.2 HBMM hard fusion

The main advantage of hard fusion schemes relative to soft fusion schemes is the low bandwidth overhead due to the transmission of a 1-bit by each SU to the fusion center. However, the local decision made by an individual SU may not always be reliable, for example, when
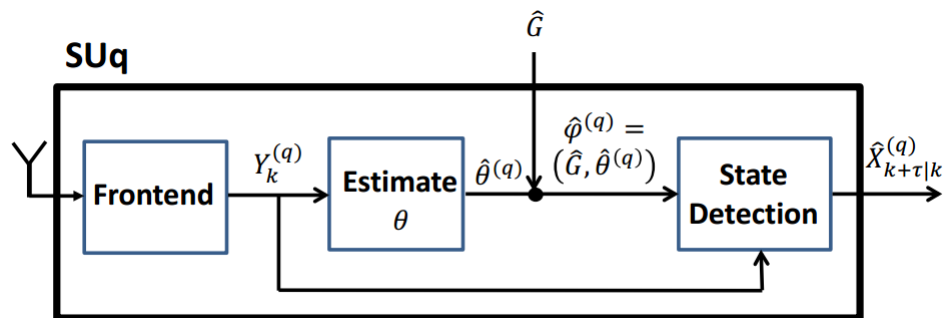
Figure 5.3: Block diagram of SU for HBMM hard fusion.

the received signal at the SU has undergone severe shadowing. Incorporating an HBMM to model the dynamics of the PU and the wireless propagation environment, can lead to much better detection performance under such conditions.

The architecture of each SUq cognitive radio transceiver in our proposed hard fusion scheme is depicted in Fig. 5.3. In this scheme, the online HBMM parameter estimation algorithm is decoupled into two parts: 1) estimating the transition matrix G and 2) estimating the parameter $\theta^{(q)}$ of the conditional output distribution for each SUq. The estimate of G can either be computed locally, based on the final decisions fed back to each SU from the fusion center, or it could be computed by the fusion center and broadcast to all SUs. Both options are equivalent with respect to estimation of G. The estimates of G are provided as input to the conditional output parameter estimation block. The transition matrix estimates are updated less frequently than the sensing decisions, so a small delay in the feedback loop from the fusion center to the SUs will not adversely affect the overall performance of the scheme. The rationale for the separating the two blocks is that estimation of θ is significantly easier than that of the transition matrix.

Consider first the conditional output density parameter estimation block for the qth SU. To simplify notation, we shall drop the superscript (q) in the following discussion. The parameter of interest, $\theta = (\theta_a : a \in \mathbb{X})$, can be estimated in a block-recursive manner using (4.8) with θ replacing ϕ, where the score function is a $1 \times 2d$ row vector given by (4.13), and $H_m(y^m; \theta)$ in (4.13) can be computed recursively using (4.22). In this case, the elements

of the $d^2r^2 \times 2d$ Jacobian matrix $\partial[\text{vec } F(y_k)]'/\partial\theta$ are given as follows:

$$\frac{\partial f_{ij}^{ab}(y_k; \theta_b)}{\partial \mu_c} = f_{ij}^{ab}(y_k; \theta_b) \cdot \frac{y_k - \mu_b}{\sigma_b^2} \mathbf{1}_{\{c=b\}},$$

$$\frac{\partial f_{ij}^{ab}(y_k; \theta_b)}{\partial \sigma_c} = f_{ij}^{ab}(y_k; \theta_b) \cdot \frac{(y_k - \mu_b)^2 - \sigma_b^2}{\sigma_b^3} \mathbf{1}_{\{c=b\}}, \tag{5.7}$$

for $c \in \mathbb{X}$, where $\mathbf{1}_A$ denotes an indicator function on set A.

Estimation of G is also performed using the recursive algorithm of Section 4.2.2. Since in estimating G, the observation data comes from the final decisions of the fusion center, the observable process Y in the recursive algorithm may be taken to be X, with values in the state-space $\mathbb{X}$, i.e., the HBMM reduces to a bivariate Markov chain. Here, the parameter $G = [g_{ab}(ij) : (a, i), (b, j) \in \mathbb{Z}]$ is estimated by using (4.8), (4.11), and (4.22), but with $f_{ij}^{ab}(y_k; \theta_b)$ in (4.19) given as follows:

$$f_{ij}^{ab}(y_k; \theta_b) = g_{ab}(ij)f(y_k; \theta_b) = g_{ab}(ij) \mathbf{1}_{\{y_k=b\}}. \tag{5.8}$$

In addition, the elements of the $d^2r^2 \times d^2r^2$ Jacobian matrix $\partial[\text{vec } F(y_{(k)})]'/\partial G$ in (4.22) are given as follows:

$$\frac{\partial f_{ij}^{ab}(y_k; \theta_b)}{\partial[g_{ce}(\iota l)]} = \mathbf{1}_{\{y_k=b, (c, \iota)=(a, i), (e, l)=(b, j)\}}, \tag{5.9}$$

for $(c, \iota), (e, l) \in \mathbb{Z}$.

Each SU computes a local estimate of the PU state based on the observation data and HBMM parameter estimate. The mean and standard deviation for the conditional density is updated after each block of observation data. Since the HBMM parameter $\phi = (\theta, G)$ is estimated online, an estimate of the state at time k, as well as a predicted estimate at time $k + \tau$, where $\tau > 0$, can be computed. The state detection scheme for the qth decision block is given formally by (4.6), dropping the superscript in the notation for $\hat{X}_{k+\tau|k}^{(q)}$. The

local SU decisions are sent to the fusion center, which then makes a final decision on the state of the PU at time k via a fusion rules. In our numerical experiments, the best performance was achieved when a linear fusion rule of the form (5.3) was used, with weights determined according to (5.4) (see Section 5.2.2).

The complexity of the conditional output density estimation block in each time slot is dominated by the computation of $H_m(y^m; \theta)$, which requires $O(d^3 r^3 \cdot 2d) = O(d^4 r^3)$ arithmetic operations. The computation of the transition matrix estimation block is dominated by the computation of $H_m(y^m; G)$, which requires $O(d^3 r^3 \cdot d^2 r^2) = O(d^5 r^5)$ arithmetic operations. Given the parameter $\phi = (\theta, G)$, the state detection scheme has complexity $O(d^2 r^2)$ [40]. Therefore, the computational complexity for each SU is $O(d^5 r^5) = O(r^5)$, when $d = 2$. Since linear fusion has complexity $O(Q)$, the overall complexity of HBMM hard fusion is given by $O(r^5 + Q)$ per time slot, which in practice reduces to $O(r^5)$.

5.3 Numerical Results

We have run simulation experiments in MATLAB to evaluate the performance of the proposed hard fusion schemes and soft fusion schemes. For the online parameter estimation algorithm given in (4.8), we set $\gamma_n = \gamma_0 n^{-\varepsilon}$ with $\gamma_0 = 0.3$ and $\varepsilon = 0.35$. We set the block size $m = 20$. The parameter space $\mathcal{G}$ and projection operator $\Pi_{\mathcal{G}}$ are the same as the temporal spectrum sensing for (4.8). To improve the convergence speed and stability, a warmup period is introduced to provide a good initial estimate for the mean and standard deviation vectors associated with the conditional density estimation block in both hard fusion scheme and soft fusion schemes. Given a sequence y^{n_0} of length $n_0 = 200$, we use the following initialization procedure:

1. Let $\mathbb{A}_1 = \{k \in \{1, \ldots, n_0\} : y_k < (\max(y^{n_0}) + \min(y^{n_0}))/2\}$ and $\mathbb{A}_2 = \{1, \ldots, n_0\} \setminus \mathbb{A}_1$.

Table 5.1: True mean and standard deviation of conditional densities.

	$(\mu_1^{(1)}, \sigma_1^{(1)})$ $(\mu_2^{(1)}, \sigma_2^{(1)})$	$(\mu_1^{(2)}, \sigma_1^{(2)})$ $(\mu_2^{(2)}, \sigma_2^{(2)})$	$(\mu_1^{(3)}, \sigma_1^{(3)})$ $(\mu_2^{(3)}, \sigma_2^{(3)})$
Scenario 1	(-105,6.32) (-88,8.94)	(-100,5.91) (-86,8.36)	(-103,6.71) (-98,8.06)
Scenario 2	(-105,6.32) (-88,8.94)	(-102,5.91) (-95,8.36)	(-103,6.71) (-98,8.06)

2. The initial estimates $\theta_a^s = (\mu_a^s, \sigma_a^s)$ are computed as follows:

$$\mu_a^s = \frac{1}{|\mathbb{A}_a|} \sum_{k \in \mathbb{A}_a} y_k, \quad \sigma_a^s = \sqrt{\frac{1}{|\mathbb{A}_a| - 1} \sum_{k \in \mathbb{A}_a} |y_k - \mu_a^s|^2}, \quad (5.10)$$

where $|\cdot|$ denotes set cardinality and $a \in \mathbb{X}$.

The initial probability vector π^s is initialized with a uniform distribution and the initial transition matrix G^s is generated randomly.

In our simulation experiments, we considered a collaboration model with three SUs (i.e., $Q = 3$). For the true parameter ϕ^0, the state transition matrix G^0 is specified by a 20×20 transition matrix given in Appendix A.1, such that $d = 2$ and $r = 10$. The true transition matrix was estimated from real spectrum measurements of a paging channel collected in [49] using the Baum algorithm. For the estimation blocks we have set $d = 2$ and $r = 10$, but a smaller value of r could be used to trade off accuracy for a reduction in computational complexity. The true mean and standard deviations of the conditional densities for three SUs are given in the Table 5.1. Two different scenarios representing different channel condition for three SUs are shown in this table.

5.3.1 Hard fusion

We evaluated the detection performance of the hard fusion scheme by applying $T = 6000$ observation samples to obtain an HBMM estimate for each SU. Each receiver operating characteristic (ROC) curve in Figs. 5.4 and 5.5 was then obtained by applying the state estimator with 10000 new observation samples. The ROC curves for various state detection
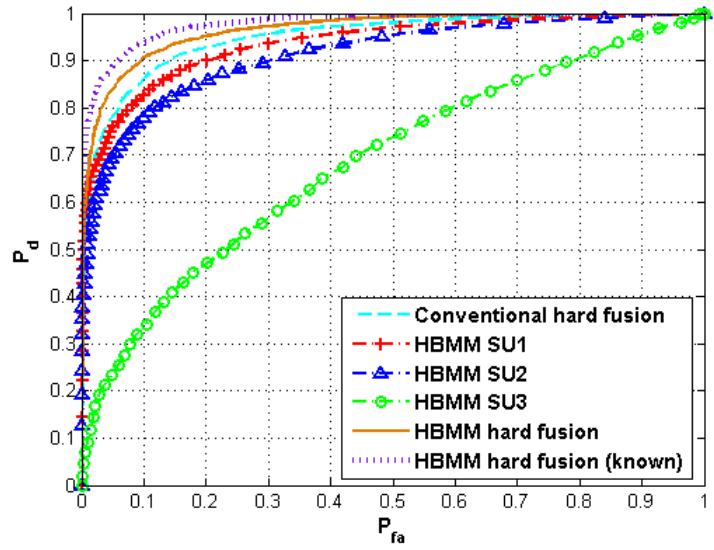
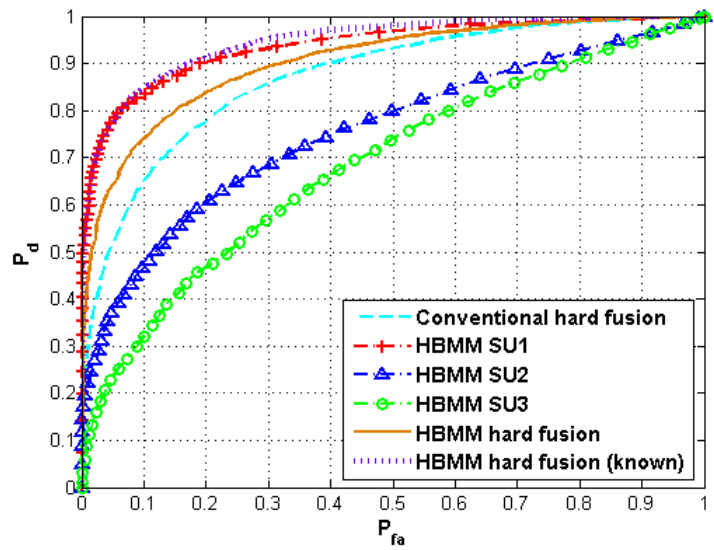Figure 5.4: ROC plot of hard fusion scheme in scenario 1.

Figure 5.5: ROC plot of hard fusion scheme in scenario 2.

schemes in scenario 1 are shown in Fig. 5.4. The vertical axis represents the probability of detection, P_d, while the horizontal axis represents the probability of false alarm, P_fa. The detection performance of each SUq, when applying HBMM state detection, is indicated as "HBMM SUq," where $q = 1, 2, 3$. The curve marked "Conventional hard fusion" was obtained using energy detectors at each SU, and a majority voting rule. The "HBMM hard fusion" curve was obtained by applying the HBMM hard fusion scheme with linear fusion and weights computed according to (5.4) with estimates of the conditional mean and standard deviation obtained from the estimation block in Fig. 5.3.

The curve marked "HBMM hard fusion (known)" is based on the same state detection scheme, but the transition matrix is assumed to be known. From Fig. 5.4 we see that, individually, SU1 and SU2 perform better than SU3 in scenario 1. In this scenario, the performance gain achievable by collaborative sensing can be seen clearly. HBMM hard fusion when the transition matrix is estimated outperforms conventional hard fusion. When the transition matrix is known, the HBMM hard fusion approach achieves even better performance.

The ROC performance for scenario 2 is shown in Fig. 5.5. From Fig. 5.5, we find SU2 and SU3 have worse performance than SU1. In this case, the performance of conventional hard fusion is inferior to that of SU1, but better than that of SU2 and SU3. The performance of the HBMM hard fusion scheme is intermediate between that of conventional hard fusion and SU1. Interestingly, when the transition matrix is known, HBMM hard fusion performs as well as SU1, or even slightly better.

5.3.2 Soft fusion

We carried out simulation experiments to compare the performance of the HBMM soft and hard fusion schemes, as well as that of the near-optimal linear soft fusion scheme developed in [44]. To apply the linear soft fusion scheme, the channel parameters are assumed to be known and the weights for linear combination and the decision threshold are computed offline according to [44]. As discussed in [52], the channel parameters can be estimated
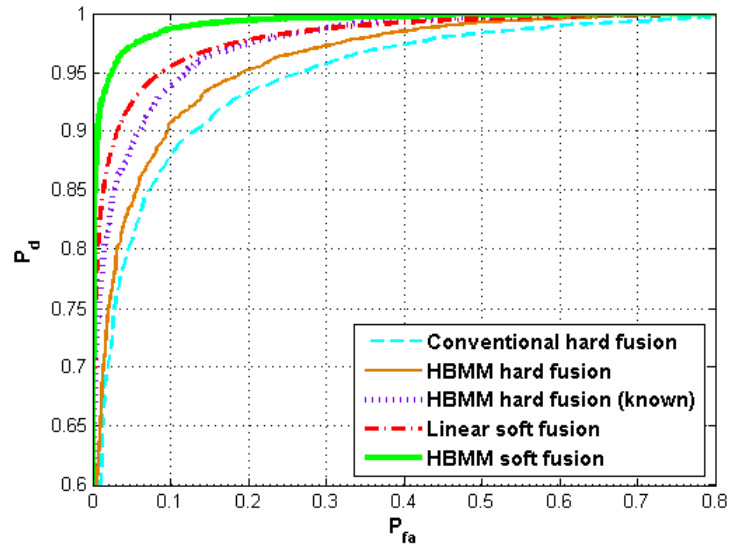
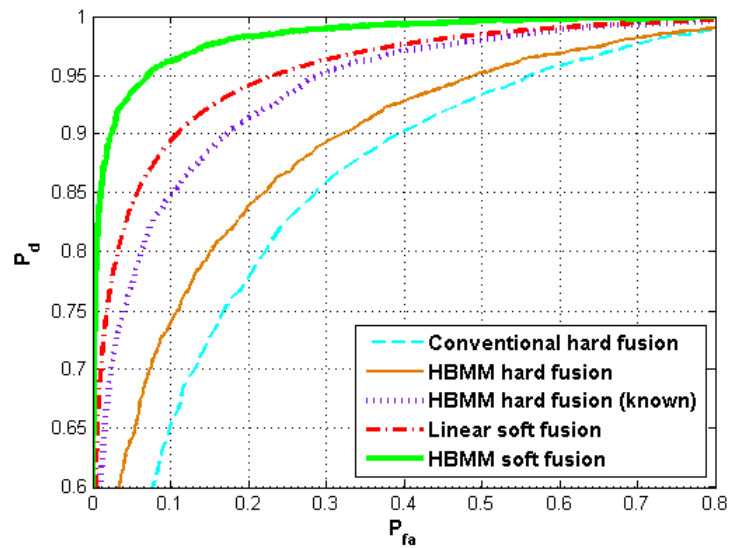Figure 5.6: ROC plot of hard and soft fusion schemes in scenario 1.

Figure 5.7: ROC plot of hard and soft fusion schemes in scenario 2.

69

online by incorporating HBMM parameter estimation, which can then be used to compute the weights and threshold for linear soft fusion in an online manner. The performance of such a scheme was found to be nearly as good as that of linear soft fusion with precomputed weights and thresholds from known channel parameters.

For scenario 1, $T = 40000$ observation samples were applied to the HBMM hard fusion, HBMM soft fusion, and linear soft fusion (with precomputed weights) schemes. A larger number of samples was used here to ensure that a sufficiently accurate estimate of the HBMM parameter could be obtained for soft fusion. The corresponding ROC curves were then computed based on 10000 subsequent observation samples, and the results are shown in Fig. 5.6. As expected, both soft fusion schemes perform significantly better than hard fusion. The computational overhead of HBMM soft fusion is higher than that of linear soft fusion when the channel parameters are assumed known, but not significantly higher when online HBMM parameter estimation is applied to update the weights and threshold. The performance of HBMM soft fusion is significantly better than linear soft fusion. Interestingly, in comparison to linear soft fusion, the performance of HBMM hard fusion is slightly worse when $P_{fa} < 0.15$, and approximately the same when $P_{fa} > 0.15$.

In scenario 2, the number of observation samples was increased to $T = 50000$. As before, 10000 additional observation samples were applied to obtain ROC curves, which are shown in Fig. 5.7. As expected, the performance for each of the collaborative sensing schemes is degraded relative to that for scenario 1. The performance gap between HBMM soft fusion and linear soft fusion is larger in scenario 2 than in scenario 1. An even larger performance gap can be seen between the linear soft fusion and hard fusion schemes for the two scenarios.

5.3.3 Predictive spectrum sensing

A useful feature of model-based spectrum sensing is the ability to predict the future state of the PU [40, 54]. A prediction of the state at a future time could be used to augment the information provided by an estimate of the current state, and thereby facilitating more proactive dynamic spectrum access. For example, even if the current state estimate indicates
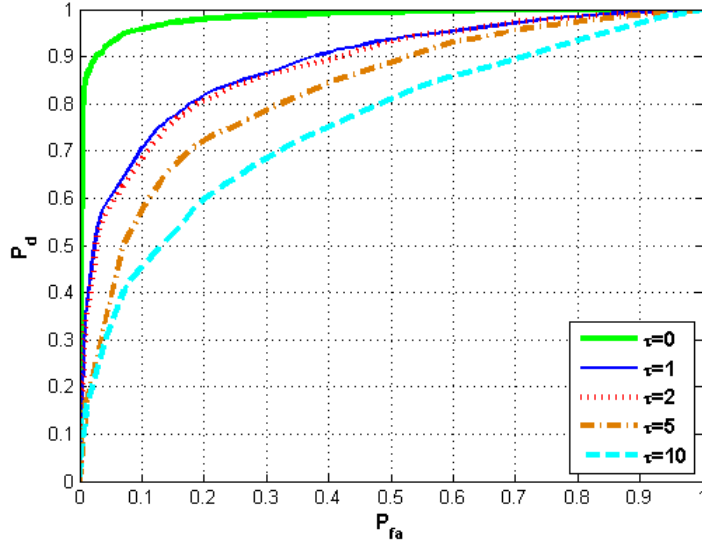
Figure 5.8: τ-step HBMM soft fusion prediction performance in scenario 2.

that the PU is idle, if the predicted state indicates that the PU will become active, an SU can vacate the channel in advance to avoid potential interference with the PU. Conversely, if the PU is detected as active in the current time slot but idle in a future time slot, an SU can proactively commence preparations for channel access in anticipation of a temporal spectrum hole. In multichannel scenarios, predictive state information can be used for selecting among multiple channels that have been detected as idle.

We ran simulation experiments to evaluate the predictive performance of the HBMM fusion scheme in scenario 2. Fig. 5.8 shows ROC curves for soft fusion prediction performance in scenario 2 for step sizes $\tau = 0, 1, 2, 5, 10$. Clearly, the prediction performance degrades as τ is increased. Interestingly, in this scenario the performance for $\tau = 2$ is nearly as good as for $\tau = 1$, though this does not hold in general. By comparing Figs. 5.7 and Fig. 5.8, we see that the performance of 1-step prediction is slightly better than state estimation using conventional hard fusion. The predictive performance of HBMM hard fusion, with unknown transition matrix, was rather poor, even for $\tau = 1$. However, when the transition matrix is known, the performance of HBMM hard fusion is quite close to that of HBMM soft fusion.
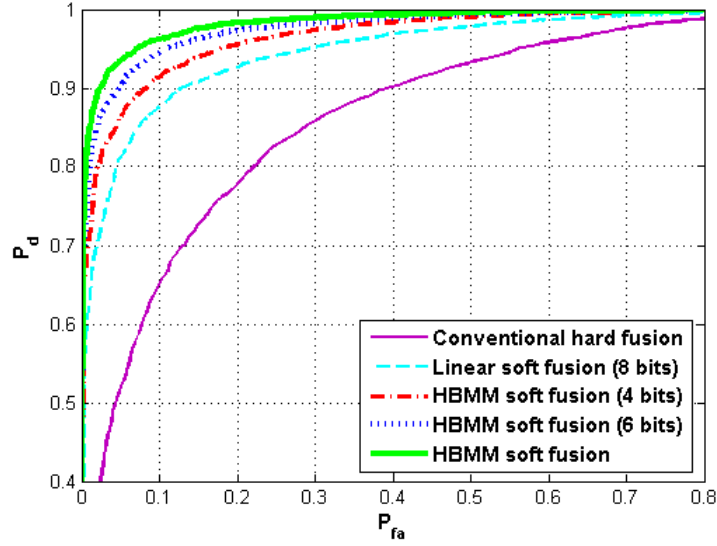
Figure 5.9: ROC plot of soft decision schemes with quantization in scenario 2.

5.3.4 Coarsely quantized soft fusion

The soft fusion experiments assumed a 32-bit representation of the observation samples, such that the bandwidth overhead was $32/\Delta$ bits/s, where Δ represents the time slot duration in seconds. The bandwidth overhead can be reduced, at the expense of detection performance, by applying coarser quantization of the observation samples. We conducted simulation experiments to evaluate the impact of coarse quantization of the observation data on the performance of the soft fusion schemes. For simplicity, we adopted a uniform quantization scheme. The quantization range for the received signal power measurements was set to $[-140, 0]$ dBm and the quantization resolution is determined by the number of bits. At each SUq, the observation sample $Y_k^{(q)}$ is quantized and encoded before being transmitted to the fusion center, which then decodes the quantized sample for further processing. In Fig. 5.9, ROC curves obtained for scenario 2 are shown for linear soft fusion with 8-bit samples and HBMM soft fusion with 4-bit and 6-bit samples. The degradation in detection performance for HBMM soft fusion can be clearly seen as the number of bits per sample is reduced from 6 to 4. We also see that HBMM soft fusion with 4-bit samples outperforms

linear soft fusion with 8-bit samples. When 3-bit samples are used, the HBMM soft fusion scheme performs worse than HBMM hard fusion.

Chapter 6: Conclusions and Future Directions

The main contribution of this thesis is to develop model-based approaches to improve the accuracy and robustness of spectrum sensing. In this concluding chapter, we present a summary of the thesis main results together with a discussion of future directions.

6.1 Spatial spectrum sensing

In spatial spectrum sensing, we were able to carry out G-MIFTP power control for SUs based on the aggregate interference analysis. Meanwhile, we employed CSMA/CA multiple access MAC protocol on each SU to avoid transmission collision between SUs. In this spatial spectrum sensing model, all SUs are distributed according to a Poisson point process, and the intensity of the Poisson point process is assumed known. It would be interesting to attempt to estimate the intensity of the Poisson point process in practical spectrum sensing scenarios. In addition, more efficient power control scheme and contention control scheme should be investigated to improve the performance of spatial spectrum sensing.

6.2 Temporal spectrum sensing

For temporal spectrum sensing, we developed an online parameter estimation algorithm to estimate the parameter of an HBMM. This online estimation algorithm is block based, and the score function for this online parameter estimation algorithm is calculated recursively. In addition, we proposed a projection mapping method for this online algorithm which improves the convergence speed and stability. Prediction of the channel occupancy behavior for the PU are also available with this estimated HBMM. The current state decision and future state prediction recusions for the PU can be used for resource allocation at the MAC

layer. For instance, an idle narrowband channel with a long available sojourn time among all the other channels can be assigned higher weight so that it would more likely be chosen by SUs, which can avoid frequent channel switching. In practice, resource allocation is much more complicated when assigning the spectrum resource to multiple SUs due to the varying channel characteristics, spectrum availability and QoS requirements. A natural extension of our work is to investigate how our proposed spectrum sensing methods can be integrated with resource allocation in a cognitive radio network.

6.3   Collaborative spectrum sensing

Collaborative spectrum sensing can improve spectrum sensing performance and alleviate the hidden terminal problem in wireless networks. In hard fusion schemes, each SU makes a hard decision on spectrum occupancy and a fusion center makes a final decision by combining the individual hard decisions according to a fusion rule. In soft fusion schemes, each SU provides a signal power measurement to the fusion center, which performs further processing on the collection of all observations to make a final decision. We proposed hard and soft fusion collaborative spectrum sensing schemes based on online hidden bivariate Markov chain modeling of the signals received by SUs. Compared to prior collaborative sensing schemes, the proposed model-based schemes do not rely on precomputed thresholds or weights, and achieve superior detection performance. A hybrid scheme, which employs HBMM soft fusion until a suitable estimate of the transition matrix is obtained and then switches to HBMM hard fusion, could provide another means of obtaining a suitable tradeoff between transmission overhead and detection performance. More efficient quantization methods can be further investigated to reduce the network overhead between the fusion center and SUs.

6.4   Software defined radio implementation

GNU radio is a free and open-source software development toolkit that provides signal processing blocks to implement a software defined radio. The USRP (Universal Software Radio

Peripheral), created by Ettus Research LLC, is the RF hardware for the software defined radio. USRP together with GNU radio are convenient hardware and software platforms for cognitive radio research. We implemented the temporal spectrum sensing on the GNU radio testbed. With the Papyrus platform which enables non-contiguous Orthogonal Frequency-Division Multiplex, we designed a traffic controller to generate the traffic trace for six PUs with the HBMM. We also implemented a dynamic accessor to perform the dynamic spectrum sensing. Then the signal strength measurement can be used for online parameter estimation for HBMM, and we obtained very satisfying performance. In the future, more work can be done on the testbed implementation to speed up the spectrum sensing. A possible approach is to implement the spectrum sensing algorithms on the FPGA directly.

Appendix A: An Appendix

A.1 20×20 **transition matrix** G

The 20×20 transition matrix G is expressed in several smaller $r \times r (r = 10)$ block matrices $G_{ab}, a, b \in \mathbb{X}$ as follows [38]:

$$
G_{11} =
\begin{bmatrix}
0.0000 & 0.2568 & 0.4256 & 0.0000 & 0.0709 & 0.0000 & 0.1027 & 0.0000 & 0.1226 & 0.0000 \\
0.0000 & 0.0000 & 0.0000 & 0.0000 & 0.0000 & 0.0000 & 0.0000 & 0.0000 & 0.0000 & 0.0000 \\
0.0000 & 0.0000 & 0.0000 & 0.0000 & 0.0000 & 0.0000 & 0.0000 & 0.0000 & 0.0000 & 0.0000 \\
0.0005 & 0.1505 & 0.1985 & 0.0000 & 0.0652 & 0.1775 & 0.1547 & 0.0154 & 0.0176 & 0.2195 \\
0.0000 & 0.0000 & 0.0000 & 0.0000 & 0.0000 & 0.0000 & 0.0000 & 0.0000 & 0.0000 & 0.0000 \\
0.0000 & 0.0094 & 0.0580 & 0.0000 & 0.0005 & 0.0000 & 0.1694 & 0.0000 & 0.0033 & 0.0000 \\
0.0000 & 0.0000 & 0.0000 & 0.0000 & 0.0000 & 0.0000 & 0.0000 & 0.0000 & 0.0000 & 0.0000 \\
0.0000 & 0.1171 & 0.3370 & 0.0000 & 0.1534 & 0.0000 & 0.1791 & 0.0000 & 0.0841 & 0.0000 \\
0.0000 & 0.0000 & 0.0000 & 0.0000 & 0.0000 & 0.0000 & 0.0000 & 0.0000 & 0.0000 & 0.0000 \\
0.0000 & 0.0353 & 0.4173 & 0.0000 & 0.0512 & 0.0000 & 0.4628 & 0.0000 & 0.0059 & 0.0000
\end{bmatrix}
$$

$$G_{12} = \begin{bmatrix}
0.0214 & 0.0000 & 0.0000 & 0.0000 & 0.0000 & 0.0000 & 0.0000 & 0.0000 & 0.0000 & 0.0000 \\
0.9008 & 0.0031 & 0.0000 & 0.0000 & 0.0210 & 0.0000 & 0.0359 & 0.0000 & 0.0001 & 0.0390 \\
0.9685 & 0.0003 & 0.0000 & 0.0000 & 0.0032 & 0.0000 & 0.0131 & 0.0000 & 0.0000 & 0.0148 \\
0.0004 & 0.0000 & 0.0000 & 0.0000 & 0.0000 & 0.0000 & 0.0000 & 0.0000 & 0.0000 & 0.0000 \\
0.9146 & 0.0046 & 0.0000 & 0.0000 & 0.0455 & 0.0000 & 0.0021 & 0.0000 & 0.0000 & 0.0332 \\
0.7594 & 0.0000 & 0.0000 & 0.0000 & 0.0000 & 0.0000 & 0.0000 & 0.0000 & 0.0000 & 0.0000 \\
0.9988 & 0.0000 & 0.0000 & 0.0000 & 0.0001 & 0.0000 & 0.0002 & 0.0000 & 0.0000 & 0.0009 \\
0.0057 & 0.0000 & 0.0000 & 0.0000 & 0.1228 & 0.0000 & 0.0003 & 0.0000 & 0.0000 & 0.0005 \\
1.0000 & 0.0000 & 0.0000 & 0.0000 & 0.0000 & 0.0000 & 0.0000 & 0.0000 & 0.0000 & 0.0000 \\
0.0165 & 0.0000 & 0.0000 & 0.0000 & 0.0106 & 0.0000 & 0.0002 & 0.0000 & 0.0000 & 0.0001
\end{bmatrix}$$

$$G_{21} = \begin{bmatrix}
0.0000 & 0.0000 & 0.0000 & 0.0000 & 0.0000 & 0.0000 & 0.0000 & 0.0000 & 0.0000 & 0.0000 \\
0.0000 & 0.0000 & 0.0000 & 0.0000 & 0.0000 & 0.0000 & 0.0000 & 0.0000 & 0.0000 & 0.0000 \\
0.0000 & 0.0000 & 0.0000 & 0.0374 & 0.0000 & 0.0000 & 0.0000 & 0.0000 & 0.0000 & 0.0000 \\
0.0003 & 0.0000 & 0.0000 & 0.0209 & 0.0000 & 0.0000 & 0.0000 & 0.0003 & 0.0000 & 0.0000 \\
0.0000 & 0.0000 & 0.0000 & 0.0000 & 0.0000 & 0.0000 & 0.0000 & 0.0000 & 0.0000 & 0.0000 \\
0.2162 & 0.0005 & 0.0003 & 0.0024 & 0.0003 & 0.0057 & 0.0001 & 0.3794 & 0.0001 & 0.1558 \\
0.0000 & 0.0000 & 0.0000 & 0.0000 & 0.0000 & 0.0000 & 0.0000 & 0.0000 & 0.0000 & 0.0000 \\
0.1308 & 0.0111 & 0.0469 & 0.0000 & 0.0207 & 0.3077 & 0.1174 & 0.0202 & 0.2828 & 0.0460 \\
0.0060 & 0.0000 & 0.0000 & 0.0000 & 0.0000 & 0.0000 & 0.0000 & 0.0000 & 0.0000 & 0.0000 \\
0.0000 & 0.0000 & 0.0000 & 0.0000 & 0.0000 & 0.0000 & 0.0000 & 0.0000 & 0.0000 & 0.0000
\end{bmatrix}$$

$$
G_{22} = \begin{bmatrix}
0.0000 & 0.0330 & 0.0002 & 0.0000 & 0.0253 & 0.0000 & 0.1454 & 0.0000 & 0.0007 & 0.7955 \\
0.0000 & 0.0000 & 0.9568 & 0.0244 & 0.0000 & 0.0007 & 0.0000 & 0.0008 & 0.0173 & 0.0000 \\
0.0000 & 0.0000 & 0.0000 & 0.8899 & 0.0000 & 0.0624 & 0.0000 & 0.0102 & 0.0000 & 0.0000 \\
0.0008 & 0.0000 & 0.0000 & 0.0000 & 0.0000 & 0.7156 & 0.0000 & 0.2620 & 0.0000 & 0.0000 \\
0.0000 & 0.0000 & 0.9349 & 0.0001 & 0.0000 & 0.0000 & 0.0000 & 0.0000 & 0.0651 & 0.0000 \\
0.0345 & 0.0000 & 0.0000 & 0.0000 & 0.0000 & 0.0000 & 0.0000 & 0.2046 & 0.0000 & 0.0001 \\
0.0000 & 0.2868 & 0.1008 & 0.0282 & 0.1979 & 0.0004 & 0.0000 & 0.0000 & 0.3859 & 0.0000 \\
0.0056 & 0.0001 & 0.0000 & 0.0000 & 0.0042 & 0.0000 & 0.0036 & 0.0000 & 0.0000 & 0.0030 \\
0.0000 & 0.0000 & 0.0510 & 0.8746 & 0.0000 & 0.0021 & 0.0000 & 0.0663 & 0.0000 & 0.0000 \\
0.0000 & 0.5373 & 0.0547 & 0.0047 & 0.0915 & 0.0151 & 0.0000 & 0.0000 & 0.2966 & 0.0000
\end{bmatrix}
$$

A.2 6×6 transition matrix G

The 6×6 transition matrix G is expressed as follows:

$$
G = \begin{bmatrix}
0.4680 & 0.0000 & 0.5319 & 0.0000 & 0.0000 & 0.0000 \\
0.5336 & 0.4664 & 0.0000 & 0.0000 & 0.0000 & 0.0000 \\
0.0000 & 0.0000 & 0.4702 & 0.0000 & 0.5297 & 0.0000 \\
0.0000 & 0.0000 & 0.0000 & 0.4543 & 0.0000 & 0.5457 \\
0.0000 & 0.0000 & 0.0000 & 0.5214 & 0.4786 & 0.0000 \\
0.0000 & 0.5302 & 0.0000 & 0.0000 & 0.0000 & 0.4698
\end{bmatrix}
$$

Bibliography

Bibliography

[1] V. Aalo and R. Viswanathan, "Asymptotic performance of a distributed detection system in correlated Gaussian noise," *IEEE Transactions on Signal Processing*, vol. 40, no. 1, pp. 211–213, Jan. 1992.

[2] I. A. Akbar and W. H. Tranter, "Dynamic spectrum allocation in cognitive radio using hidden Markov models: Poisson distributed case," in *Proc. IEEE SoutheastCon*, pp. 196–201, March 2007.

[3] I. F. Akyildiz, W.-Y. Lee, and M. C. Vuran, "Next generation/dynamic spectrum access/cognitive radio wireless networks: A survey," *Computer Networks*, vol. 50, no. 13, pp. 2127–2159, May. 2006.

[4] F. Baccelli and B. Blaszczyszyn, "Stochastic geometry and wireless networks, Volume 1: Theory," *Foundation and Trends in Networking*, vol. 3, no. 3-4, pp. 249–449, Jan. 2009.

[5] L. E. Baum and T. Petrie, "Statistical inference for probabilistic functions of finite state Markov chains," *Annals of Mathematical Statistics*, vol. 37, no. 6, pp. 1554–1563, Apr. 1966.

[6] Y. Chen, G. Yu, and Z. Zhang, "On cognitive radio networks with opportunistic power control strategies in fading channels," *IEEE Trans. on Wireless Communications*, vol. 7, no. 7, pp. 2752–2761, July 2008.

[7] Z. Chen, C.-X. Wang, and X. Hong, "Aggregate Interference Modeling in Cognitive Radio Networks with Power and Contention Control," *IEEE Trans. on Communications*, vol. 60, no. 2, pp. 456–468, Feb. 2012.

[8] A. P. Dempster, N. M. Laird, and D. B. Rubin, "Maximum likelihood from incomplete data via the EM algorithm," *J. Royal Stat. Soc.*, vol. 39, pp. 1–38, 1977.

[9] C. Y. Edward, Y. Liang, and Y. L. Guan, "Cooperative Spectrum Sensing in Cognitive Radio Networks with Weighted Decision Fusion Schemes," *IEEE Trans. on Wireless Communications*, vol. 9, no. 12, pp. 3838–3847, Dec. 2010.

[10] Y. Ephraim and B. L. Mark, "Bivariate Markov processes and their estimation," *Foundations and Trends in Signal Processing*, vol. 6, no. 1, pp. 1–95, June 2013.

[11] Y. Ephraim and N. Merhav, "Hidden Markov processes," *IEEE Transactions on Information Theory*, vol. 48, no. 6, pp. 1518–1569, June 2002.

[12] FCC, "Spectrum Policy Task Force," Nov. 2002.

[13] S. Geirhofer, L. Tong, and B. M. Sadler, "Dynamic spectrum access in the time domain: Modeling and exploiting white space," *IEEE Communications Magazine*, vol. 45, no. 5, pp. 66–72, May 2007.

[14] A. Ghasemi and E. S. Sousa, "Interference Aggregation in Spectrum-Sensing Cognitive Wireless Networks," *IEEE Journal of Selected Topics in Signal Processing*, vol. 2, no. 1, pp. 41–56, Feb. 2008.

[15] C. Ghosh, C. Cordeiro, D. P. Agrawal, and M. B. Rao, "Markov chain existence and hidden Markov models in spectrum sensing," in *Proc. IEEE Int. Conf. on Pervasive Computing and Communications (PerCom)*, pp. 1–6, March 2009.

[16] M. Gudmundson, "Correlation model for shadow fading in mobile radio systems," *Electron. Lett.*, vol. 47, pp. 2145–2146, Nov. 1991.

[17] M. Haenggi, "Mean Interference in Hard-Core Wireless Networks," *IEEE Communications Letters*, vol. 15, no. 8, pp. 792–794, Jun. 2011.

[18] K. Haghighi, E. G. Ström, and E. Agrell, "On optimum causal cognitive spectrum reutilization strategy," *IEEE Journal on Selected Areas in Communications*, vol. 30, no. 10, pp. 1911–1921, Nov. 2012.

[19] U. Holst and G. Lindgren, "Recursive estimation in mixture models with Markov regime," *IEEE Transactions on Information Theory*, vol. 37, no. 6, pp. 1683–1690, Nov. 1991.

[20] H. Islam, Y.-C. Liang, and A. Hoang, "Joint power control and beamforming for cognitive radio networks," *IEEE Trans. on Wireless Communications*, vol. 7, no. 7, pp. 2415–2419, July 2008.

[21] R. Kashyap and R. Chellappa, "Stochastic Models for Closed Boundary Analysis: Representation and Reconstruction," *IEEE Trans. on Information Theory*, vol. 27, no. 5, pp. 627–637, Sep. 1981.

[22] S. M. Kay, *Fundamentals of Statistical Signal Processing: Detection Theory*. Englewood Cliffs, NJ: Prentice-Hall, 1998.

[23] H. Kobayashi, B. L. Mark, and W. Turin, *Probability, Random Processes, and Statistical Analysis*. Cambridge, UK: Cambridge University Press, 2012.

[24] B. Kouassi, L. Deneire, and B. Zayen, "Design and Implementation of Spatial Interweave LTE-TDD Cognitive Radio Communication on an Experimental Platform," *IEEE Wireless Communications*, vol. 20, no. 2, pp. 60–67, Apr. 2013.

[25] V. Krishnamurthy and J. Moore, "On-line estimation of hidden Markov model parameters based on the Kullback-Leibler information measure," *IEEE Transactions on Signal Processing*, vol. 41, no. 8, pp. 2557–2573, Aug. 1993.

[26] G. Latouche and V. Ramaswami, *Introduction to matrix analytic methods in stochastic modeling*. ASA/SIAM Series on Statistics and Applied Probability, 1999.

[27] F. LeGland and L. Mevel, "Recursive estimation in hidden Markov models," in *Proc. 36th IEEE Conference on Decision and Control*, vol. 4, pp. 3468–3473, Dec. 1997.

[28] A. E. Leu, B. L. Mark, and M. A. McHenry, "A framework for cognitive WiMAX with frequency agility," *Proc. IEEE, Special Issue on Cognitive Radio*, vol. 97, no. 4, pp. 755–773, Apr. 2009.

[29] A. E. Leu, M. McHenry, and B. L. Mark, "Modeling and analysis of interference in Listen-Before-Talk spectrum access schemes," *Int. J. Network Mgmt.*, vol. 16, no. 2, pp. 131–141, Mar. 2006.

[30] B. Li, C. Zhao, M. Sun, Z. Zhou, and A. Nallanathan, "Spectrum sensing for cognitive radios in time-variant flat fading channels: A joint estimation approach," *IEEE Trans. on Communications*, vol. 62, no. 8, pp. 2665–2680, Aug. 2014.

[31] M. N. Lustgarten and J. A. Madsen, "An Empirical Propagation Model (EPM-73)," *IEEE Trans. on Electromagnetic Compatibility*, vol. 19, Aug. 1977.

[32] J. Ma, G. Zhao, and Y. Li, "Soft Combination and Detection for Cooperative Spectrum Sensing in Cognitive Radio Networks," *IEEE Trans. on Wireless Communications*, vol. 7, no. 11, pp. 4502–4507, Nov. 2008.

[33] B. L. Mark and A. E. Leu, "Local averaging for fast handoffs in cellular networks," *IEEE Transactions on Wireless Communications*, vol. 6, no. 3, pp. 866–874, March 2007.

[34] B. L. Mark and A. O. Nasif, "Estimation of maximum interference-free transmit power level for opportunistic spectrum access," *IEEE Transactions on Wireless Communications*, vol. 8, no. 5, pp. 2505–2513, May 2009.

[35] J. W. Mark and W. Zhuang, *Wireless Communications and Networking*. Pearson Education, Inc., 2003.

[36] M. McHenry, K. Steadman, and A. E. Leu, "XG DSA Radio System," *IEEE Symposium on DySPAN*, pp. 1–11, Oct. 2008.

[37] M. F. Neuts, *Matrix-Geometric Solutions in Stochastic Models*. Baltimore: Johns Hopkins University Press, 1981.

[38] T. Nguyen, *Hidden Markov model based spectrum sensing for cognitive radio*. PhD thesis, Dept. of Electrical and Computer Engineering, George Mason University, Apr. 2013.

[39] T. Nguyen, B. L. Mark, and Y. Ephraim, "Hidden Markov process based dynamic spectrum access for cognitive radio," in *Proc. Conference on Information Sciences and Systems (CISS)*, (Baltimore, MD), pp. 1–6, Mar. 2011.

[40] T. Nguyen, B. L. Mark, and Y. Ephraim, "Spectrum sensing using a hidden bivariate Markov model," *IEEE Transactions on Wireless Communications*, vol. 12, no. 9, pp. 4582–4591, Aug. 2013.

[41] T. V. Nguyen and F. Baccelli, "A stochastic geometry model for cognitive radio networks," *The Computer Journal*, vol. 55, no. 5, pp. 534–552, Jul. 2012.

[42] P. Pawelczak, "Cognitive Radio: Ten years of Experimentation and Development," *IEEE Commun. Mag.*, vol. 49, no. 3, pp. 90–100, Apr. 2011.

[43] E. Peh, Y.-C. Liang, Y. L. Guan, and Y. Zeng, "Cooperative Spectrum Sensing in Cognitive Radio Networks with Weighted Decision Fusion Schemes," *IEEE Trans. on Wireless Communications*, vol. 9, no. 12, pp. 3838–3847, Dec. 2010.

[44] Z. Quan, W.-K. Ma, and S. Cui, "Optimal linear cooperation for spectrum sensing in cognitive radio networks," vol. 2, no. 1, pp. 28–40, Feb. 2008.

[45] A. Rabbachin, T. Q. Quek, and H. Shin, "Cognitive Network Interference," *IEEE Trans. on Selected Areas in Communications*, vol. 29, no. 2, pp. 480–493, Feb. 2011.

[46] W. Ren, Q. Zhao, and A. Swami, "Power control in spectrum overlay networks: How to cross a multi-lane highway," *IEEE J. Sel. Areas Commun*, vol. 27, no. 7, pp. 1283–1296, Sep. 2009.

[47] T. Rydén, "On recursive estimation for hidden Markov models," *Stochastic Processes and their Applications*, vol. 66, no. 1, pp. 79–96, Feb. 1997.

[48] H. A. B. Salameh and M. M. Krunz, "MAC Protocol for Opportunistic Cogntive Radio Networks with Soft Guarantees," *IEEE Transcations on Mobile Computing*, vol. 8, no. 10, pp. 1339–1352, Oct. 2009.

[49] Shared Spectrum Company, "General Survey of Radio Frequency Bands: 30 MHz to 3 GHz," Tech. Rep., August 2010.

[50] S. Srinivasa and S. A. Jafar, "Soft Sensing and Optimal Power Control for Cognitive Radio," *IEEE Trans. on Wireless Communications*, vol. 9, no. 12, pp. 3638–3649, Dec. 2010.

[51] D. Stoyan, W. S. Kendall, and J. Mecke, *Stochastic Geometry and its Applications*. New York: Wiley, 2 Edition, 1996.

[52] Y. Sun, B. L. Mark, and Y. Ephraim, "Collaborative Spectrum Sensing Based on Hidden Bivariate Markov Models," *IEEE GC 2015 Workshop on Emerging Technologies for 5G Wireless Cellular Networks*, Dec. 2015 (to appear).

[53] Y. Sun and B. L. Mark, "Interference model for spectrum sensing with power control," in *Proc. of Conference on Information Science and Systems (CISS)*, (Baltimore, MD), pp. 1–6, Mar. 2013.

[54] Y. Sun, B. L. Mark, and Y. Ephraim, "Online parameter estimation for temporal spectrum sensing," *IEEE Transactions on Wireless Communications*, vol. 14, no. 8, pp. 4105–4114, Mar. 2015.

[55] Y. Sun, B. L. Mark, and Y. Ephraim, "Collaborative Spectrum Sensing via Online Estimation of Hidden Bivariate Markov Models," *IEEE Transactions on Wireless Communications*, Sep. 2015 (under review).

[56] Z. Sun, G. Bradford, and N. Laneman, "Sequence detection algorithms for PHY-layer sensing in dynamic spectrum access networks," vol. 5, no. 1, pp. 97–109, February 2011.

[57] K. W. Sung, S.-L. Kim, and J. Zander, "Temporal spectrum sharing based on primary user activity prediction," *IEEE Transactions on Wireless Communications*, vol. 9, no. 12, pp. 3848–3855, Dec. 2010.

[58] C. J. Willy, W. J. J. Roberts, and T. A. Mazzuchi, "Recursions for the MMPP score vector and observed information matrix," *Stochastic Models*, vol. 26, no. 4, pp. 649–665, July 2010.

[59] T. Yucek and H. Arslan, "A Survey of Spectrum Sensing Algorithms for Cognitive Radio Applications," *IEEE Communications Surveys and Tutorials*, vol. 11, no. 1, pp. 116–130, Mar. 2009.

[60] Q. Zhao and B. M. Sadler, "A Survey of Dynamic Spectrum Access," *Signal Process Magazine*, vol. 24, no. 3, pp. 79–89, May 2007.

Curriculum Vitae

Yuandao Sun received the M.S. degree in Electrical and Computer Engineering from Tongji University, Shanghai, China, and the B.S. degree in Electronics and Information Engineering from Zhejiang Gongshang University, Hangzhou, China. He is currently pursuing the Ph.D. degree in Electrical and Computer Engineering at George Mason University, Fairfax, Virginia. His current research interests include wireless communications, signal processing, and cognitive radio technology.